RSC Advances

PAPER

View Article Online
View Journal | View Issue

Cite this: *RSC Adv.*, 2026, **16**, 18311

A green and facile modification of red mud waste with MIL-100 (Fe) for multi-pollutant adsorption from wastewater: isotherms, kinetics, and thermodynamics

Adarsh Singh,[a] Manne Chimyang,[a] Akash Rawat,[b] Venkatesh Uddameri[c] and Ashok Kumar Gupta *[a]

The expansion of the textile and pharmaceutical industries, driven by rapid population growth and evolving lifestyles, has led to an increased release of synthetic chemicals into the environmental matrices, thereby posing risks to aquatic ecosystems and human health. A novel composite adsorbent, fabricated by integrating thermally activated red mud (ARM) with MIL-100 (Fe) (referred to as MARM) *via* co-precipitation, was utilized for the adsorptive removal of methylene blue (MLB), Congo red (CNR), and levofloxacin (LVX) from an aqueous solution. The assessment of textural properties showed MARM-II (containing 40% MIL-100 Fe) with a high specific surface area (SSA) of 651.741 m^2 g^{-1}. The enhanced SSA and distinctive surface charge profile of MARM-II promoted the effective adsorption of MLB, CNR, and LVX onto the MARM-II surface. At optimal conditions (contact time: 150 min, initial MLB, CNR, and LVX concentration: 10 mg L^{-1} each, MARM-II dose: 0.4 g L^{-1}, solution pH: 7, and temperature: 27 ± 3 °C), MLB, CNR, and LVX removals were recorded to be 93.077 ± 0.593%, 89.739 ± 1.119%, and 96.102 ± 0.997%, respectively. The pseudo-second-order kinetic model confirmed chemisorption was the governing mechanism, while the Sips isotherm best explained the adsorptive nature of MLB, CNR, and LVX on the surface of MARM-II composite. The maximum adsorption capacity for MLB, CNR, and LVX was found to be 123.021 ± 11.926, 143.934 ± 24.248, and 97.657 ± 5.686 mg g^{-1}, respectively. Additionally, the thermodynamic investigation indicates that the adsorption process was characterized as exothermic and spontaneous. The mechanistic insights showcased that the adsorption process was mainly driven by electrostatic interaction, hydrogen bonding, π–π interaction, and chemisorption.

Received 24th January 2026
Accepted 23rd March 2026

DOI: 10.1039/d6ra00635c

rsc.li/rsc-advances

1. Introduction

The decline in the quality of water resources caused by the release of organic pollutants from various industrial and domestic sources has become a significant environmental issue.[1] Synthetic dyes, including methylene blue (MLB) and Congo red (CNR), are widely utilized in the textile, printing, and pharmaceutical sectors, resulting in their significant presence in the effluent from these industries.[2] In addition, the wastewater discharged from domestic households and healthcare facilities often contains antibacterial drugs like levofloxacin (LVX), which also contributes to surface water contamination.[3] Reportedly, the abovementioned compounds (MLB, CNR, and LVX) are recalcitrant to biodegradation owing to their xenobiotic nature.[4–6] Organic dyes contribute to the coloration of water, which obstructs light penetration, consequently diminishing photosynthesis and oxygen solubility.[7] Additionally, they have been documented to possess mutagenic and carcinogenic potential.[8] Moreover, LVX is a fluoroquinolone-based antibiotic that acts against both Gram-positive and Gram-negative bacteria, along with pathogens.[9] Thus, if released into aquatic environments, it possesses bioaccumulation potential,[10] thereby threatening aquatic biota. Therefore, there is a prompt need for efficient treatment processes capable of eliminating such recalcitrant and toxic chemicals.

Adsorption has emerged as a prominent method for eliminating a wide range of pollutants from water and wastewater because of its high efficiency, simplicity, cost-effectiveness, and versatility.[11–15] Lately, several adsorbents have been studied for the elimination of dyes and pharmaceuticals from aqueous matrices, including metal–organic frameworks (MOFs),[11] metal oxides,[16] zeolites,[17] activated carbon,[18] polymer-based substances,[19] and layered double hydroxide (LDH)-based materials.[20–22] Among these materials, MOFs have attracted

[a]*Environmental Engineering Division, Department of Civil Engineering, Indian Institute of Technology Kharagpur, Kharagpur 721302, India. E-mail: agupta@civil.iitkgp.ac.in*

[b]*School of Environmental Science and Engineering, Indian Institute of Technology Kharagpur, Kharagpur 721302, India*

[c]*Department of Civil and Environmental Engineering, Lamar University, Beaumont, TX 77701, USA*

significant attention for adsorption applications, owing to advances in their design and synthesis.[23] These porous materials consist of metal nodes and organic ligands, and showcase remarkable properties such as high porosity, pore size tunability, and a high specific surface area (SSA).[24] Over the years, a wide range of MOFs, based on Al, Co, Cu, Cr, Fe, and other metals, as well as their composites, have been utilized.[25–27] Unlike other MOFs, Fe-based MOFs stand out owing to the abundance of Fe on Earth,[28] its relatively low toxicity, and eco-friendly nature.[26]

Specifically, MIL-100 (Fe) possesses high stability due to a rigid zeo-type structure consisting of octahedral Fe(III) and trimesic acid.[29] However, the precisely defined structure of MOFs results in a fixed density of adsorption sites, which ultimately establishes an upper limit on their adsorption capacity.[30] This limitation opens up opportunities to incorporate complementary materials that can enhance the adsorption capacity of MOF-based composites. In the context of environmental applications, the development of such composites is expected to follow principles of simplicity, versatility, economic viability, and sustainability.[26] Notably, if the complementary material is derived from waste, it justifies the highest priority for use owing to both economic and environmental benefits. Given this perspective, red mud (RM) presents itself as an effective candidate for consideration, as it is a by-product produced during the refining of bauxite ore for alumina production.[31] The global annual discharge of RM into the environment is approximately 120 million tons.[32] Disposing of RM poses a significant environmental challenge, especially in regions with active alumina industries, due to its extreme alkalinity.[33] Before 1970, alumina producing industries released RM into marine environments; however, this practice transitioned to disposal on land, notably dry stacking, in response to ecological problems.[34,35] RM primarily comprises a metal-rich matrix, which includes key compounds, such as Fe_2O_3, Al_2O_3, and SiO_2.[36,37] Although RM has found applications in construction materials, ceramics, and surface treatment for carbon steel, its use as a low-cost adsorptive material for eliminating pollutants from aqueous matrices has garnered significant attention but has not been fully explored.[38]

A sustainable and cost-effective activated RM (ARM) and MIL-100 (Fe) composite (referred to as MARM hereafter) was developed in this study using a facile synthesis process at ambient temperature, anticipating synergistic interfacial interactions between the constituent materials (Fig. 1). The as-synthesized adsorptive materials were extensively characterized to investigate their crystallinity, functional groups and molecular vibrations, surface morphology and topography, elemental composition, local chemical environment, textural properties, thermal and chemical stability, and microstructural features at high resolution. Subsequently, MARM composite was employed for the adsorption of a mixture of MLB, CNR, and LVX from aqueous solution under varying operational conditions, including contact time, initial adsorbate concentration, adsorbent dosage, solution pH, and temperature. The possible impact of co-existing ions and the real wastewater matrix was evaluated to assess the applicability of the MARM-II condition under field conditions. The adsorptive potential was assessed through kinetic, isotherm, and thermodynamic analyses. A proposed sorption mechanism was subsequently proposed, along with a desorption and reusability study to assess the composite's stability and durability. Finally, an economic analysis of the MARM-II composite was done to evaluate its practical feasibility.

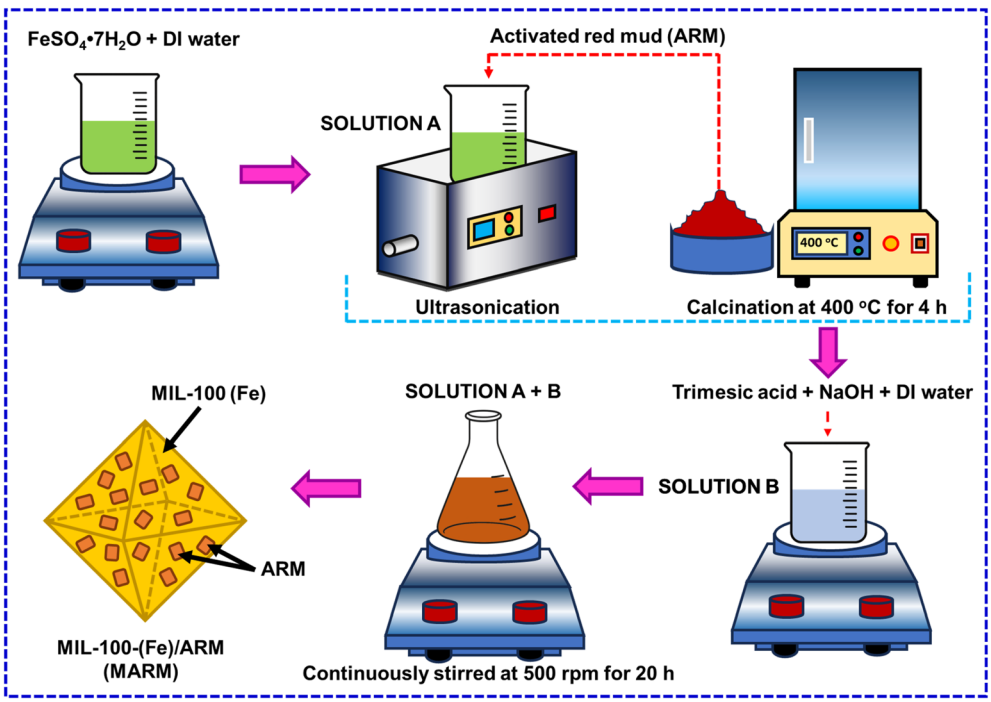

Fig. 1 Schematic representation of the preparation method for MIL-100 (Fe)/ARM (MARM) composites.

2. Experimental section

2.1. Chemicals and reagents

The chemicals and reagents used in this study have been numbered in Table S1. All chemicals were of reagent grade with purity >98%.

2.2. Analytical and instrumentation techniques

The instruments deployed in the present study for characterizing as-prepared adsorptive materials and aliquot measurement have been enumerated in Table S2.

2.3. Preparation of ARM integrated with MIL-100 (Fe) (referred to as MARM)

The pH of the raw RM sample was brought close to 7 through repeated ultrasonic-assisted dispersion, stirring, and decanting.[37] Thereafter, the RM sample was thermally activated (referred to as ARM) by calcining it at 400 °C for 4 h.[39] At first, 2.25 g of ferrous heptahydrate ($FeSO_4 \cdot 7H_2O$) was dissolved in 125 mL of deionized (DI) water to form a homogenous solution (labeled as solution A). A predetermined amount of ARM was then ultrasonically dispersed in solution A, and continuously stirred for 3 h at 60 °C. Concurrently, 1.42 g of benzene-1,3,5-tricarboxylic acid or trimesic acid (H_3BTC) and 0.80 g of sodium hydroxide (NaOH) were added to 125 mL of deionized (DI) water and subjected to ultrasonication until a clear solution was obtained (labeled as solution B). Subsequently, both solutions (A and B) were transferred to a 500 mL Erlenmeyer flask and stirred at 500 rpm for 20 h, facilitating a reaction in the presence of air. After the end of reaction period, the precipitate was filtered and rinsed three times using ethanol and DI water, alternatively. The end product, a brownish-orange colored powder (labeled as MARM-I, MARM-II, and MARM-III, corresponding to 80%, 60%, and 40% ARM added relative to $FeSO_4 \cdot 7H_2O$, respectively), was obtained after overnight drying at 60 °C, followed by heating at 100 °C for 6 h. Pristine MIL-100 (Fe) was prepared following a similar route, excluding the addition of ARM, utilizing a previously reported method.[40]

2.4. Adsorption studies

The adsorption experiments were performed in batch mode using a 250 mL borosilicate Erlenmeyer flask. It contained specific dosages of MARM-II and various initial concentrations of LVX, MLB, and CNR, with the solution pH adjusted to 7 ± 0.1. The solution pH was adjusted using 0.1 M NaOH or HCl solution. The varied concentrations of the aforesaid contaminants were achieved by diluting 500 mg L^{-1} of LVX, MLB, and CNR stock solutions. The physicochemical properties of LVX, MLB, and CNR stock solutions are described in Table 1. The experimental sample was stirred at 200 rpm on a digital multi-position hot plate stirrer at ambient temperature (27 ± 3 °C), unless otherwise specified. At predetermined time intervals, a sample was withdrawn from the solution mixture, and the adsorbent was set apart by centrifugation at 10 000 rpm for 10 min. A UV-vis spectrophotometer was utilized to analyze the concentration of LVX, MLB, and CNR in the aliquot at wavelengths around 288 nm, 664 nm, and 497 nm, respectively. A series of dilutions was prepared from the mixed stock solution, each containing 500 mg L^{-1} of LVX, MLB, and CNR. Calibration curves for each analyte showcased excellent linearity with determination coefficients ($R^2 > 0.99$). Each set of experiments was done in triplicate, and the extent of LVX, MLB, and CNR removal (η) was calculated as follows (eqn (1)):

$$\eta(\%) = \left[1 - \left(\frac{C_t}{C_0}\right)\right] \times 100 \quad (1)$$

where, C_0 and C_t are the initial LVX, MLB, and CNR concentrations, and at equilibrium time 't', expressed in mg L^{-1},

Table 1 Physicochemical properties of MLB, CNR, and LVX[131]

Physicochemical properties	MLB	CNR	LVX
Chemical formula	$C_{16}H_{18}N_3SCl$	$C_{32}H_{22}N_6Na_2O_6S_2$	$C_{18}H_{20}FN_3O_4$
Molecular structure	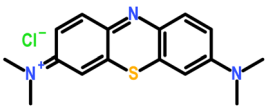	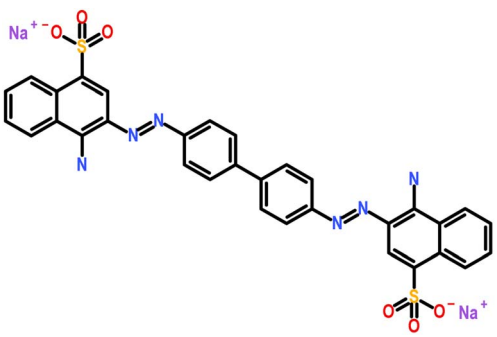	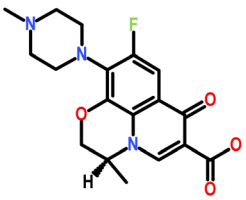
Molar mass	319.9 g mol^{-1}	696.7 g mol^{-1}	361.4 g mol^{-1}
Ionic behavior	Cationic	Anionic	—
Maximum detection wavelength (λ_{max})	664 nm	498 nm	288 nm

respectively. Moreover, the adsorption capacity (q_t) at time 't' was quantified as follows (eqn (2)):

$$q_t = \frac{(C_0 - C_t)V}{m} \quad (2)$$

where, V is the volume of the solution in 'L', and m is the mass of the adsorbent in 'g'.

2.5. Adsorption kinetics

The adsorption kinetics elucidate the rate and mechanism of the adsorptive process involving various physicochemical interactions between the adsorbent and adsorbate interface. Therefore, the time-resolved adsorption data of LVX, MLB, and CNR were fitted in various kinetic models, *i.e.*, pseudo-first-order (PFO),[41] pseudo-second-order (PSO),[42] Elovich,[43] and intraparticle diffusion (IPD) models,[44] to determine the governing mechanism of the adsorption process (eqn (3)–(6)).

$$q_t = q_e(1 - e^{-k_1 t}) \quad (3)$$

$$q_t = \frac{k_2 q_e^2 t}{q_e k_2 t + 1} \quad (4)$$

$$q_t = \frac{1}{\beta}\ln(1 + \alpha\beta t) \quad (5)$$

$$q_t = k_i t^{1/2} + c \quad (6)$$

where, q_t (mg g^{-1}) and q_e (mg g^{-1}) are the adsorption capacity at time 't' and equilibrium condition, respectively; k_1 (min^{-1}), k_2 (g mg^{-1} min^{-1}), k_i (mg g^{-1} min$^{-0.5}$), α (mg g^{-1} min^{-1}), and β (g mg^{-1}) are the PFO, PSO, IPD, initial sorption, and desorption rate constants, respectively; and c is the boundary layer thickness.

2.6. Adsorption isotherms

The interaction between adsorbate and adsorbent surface under equilibrium conditions could be interpreted through isotherm studies. The equilibrium data were fitted to various adsorption isotherm models, including Langmuir,[45] Freundlich,[46] Sips,[47] and Redlich–Peterson isotherms,[48] to analyze the adsorptive potential of LVX, MLB, and CNR molecules on MARM-II composite (eqn (7)–(10)).

$$q_e = \frac{Q_{max} K_L C_e}{1 + K_L C_e} \quad (7)$$

$$q_e = K_F C_e^{1/n} \quad (8)$$

$$q_e = \frac{Q_m K_s C_e^{m}}{1 + K_s C_e^{m}} \quad (9)$$

$$q_e = \frac{K_{RP} C_e}{1 + \alpha_{RP} C_e^{\beta}} \quad (10)$$

where, Q_{max} (mg g^{-1}) is the maximum monolayer adsorption capacity as depicted by the Langmuir model, C_e (mg L^{-1}) refers to the equilibrium concentration of the adsorbate, while K_L (L mg^{-1}) is the Langmuir isotherm constant, which represents the affinity between the adsorbate and the adsorbent. The Freundlich constant, K_F [(mg g^{-1}) (L mg^{-1})$^{1/n}$] corresponds to the adsorption capacity of the adsorbent, and n (dimensionless) is the Freundlich heterogeneity factor, indicative of the intensity and non-ideality of adsorption on heterogeneous surfaces. K_s (L mg^{-1})^m depicts the Sips equilibrium constant, and m (dimensionless) is the Sips isotherm exponent (For $m = 1$, the Sips equation (eqn (9)) converges to the Langmuir model, and at low equilibrium concentrations ($C_e \rightarrow 0$), it simplifies to the Freundlich model). Further, K_{RP} (L mg^{-1}) refers to the Redlich–Peterson isotherm constant, and α_{RP} (L mg^{-1})$^\beta$ is the Redlich–Peterson constant, where β ranges between 0 and 1 (For $\beta = 1$, the Redlich–Peterson equation (eqn (10)) simplifies to the Langmuir model, whereas at high equilibrium concentrations ($C_e \rightarrow \infty$), it approximates the Freundlich model, depicting both monolayer and heterogeneous adsorptive behaviors.

2.7. Adsorption thermodynamic studies

The impact of temperature on the adsorptive removal of LVX, MLB, and CNR using MARM-II composite was examined by thermodynamic assessment.[49,50] The thermodynamic parameters, including changes in standard Gibbs' free energy ($\Delta G°$) (kJ mol^{-1}), entropy ($\Delta S°$) (J K^{-1} mol^{-1}), and enthalpy ($\Delta H°$) (kJ mol^{-1}), were obtained through the following equations (eqn (11) and (12)):

$$\Delta G^\circ = -RT\ln K_e^\circ \quad (11)$$

$$\ln K_e^\circ = -\frac{\Delta H^\circ}{RT} + \frac{\Delta S^\circ}{R} \quad (12)$$

where, R (8.314 J mol^{-1} K^{-1}) is the universal gas constant, T (K) represents temperature, and K_e° (dimensionless) is the thermodynamic equilibrium constant.

2.8. Stability and reusability studies

The thermal stability of the MARM-II composite was assessed deploying thermogravimetric analysis (TGA) and differential thermal analysis (DTA). In addition, the possible leaching of metals and organic linker from the MARM-II composite in the treated solution was quantified using inductively coupled plasma mass spectrometry (ICP-MS), and total organic carbon (TOC) analysis, respectively. Furthermore, the regenerative ability and repeated application of MARM-II were evaluated by a reusability test. Subsequent to each batch experiment, the exhausted MARM-II composite was suspended in 0.5 M HCl and agitated at 200 rpm for 90 min, followed by an analogous procedure with 0.5 M NaOH and acetone.[19,51] Subsequently, the adsorbent was collected, washed, and dried as previously reported to neutralize the pH. The adsorptive removal of LVX, MLB, and CNR was quantified after each cycle, up to five successive cycles. Then, its diffractogram and FTIR spectra were acquired to examine any changes in the crystallographic properties and chemical composition of the MARM-II composite, respectively.

3. Results and discussion

3.1. Characterization of the pristine and composite adsorptive materials

The crystalline nature of the as-synthesized adsorbents was investigated by X-ray diffraction spectroscopy (XRD). As displayed in Fig. 2a, MIL-100 (Fe) exhibited Bragg peaks at $2\theta \sim 10.37°$, 11.03°, 12.55°, 14.27°, 20.15°, and 24.15°, aligning with the existing literature.[52,53] In the diffractogram of ARM, the peaks observed at $2\theta \sim 12.34°$ and 24.91° can be assigned to the kaolinite phase,[54] while the peak at $2\theta \sim 26.64°$ relates to the quartz phase.[55] Moreover, the peaks determined at $2\theta \sim 24.20°$,

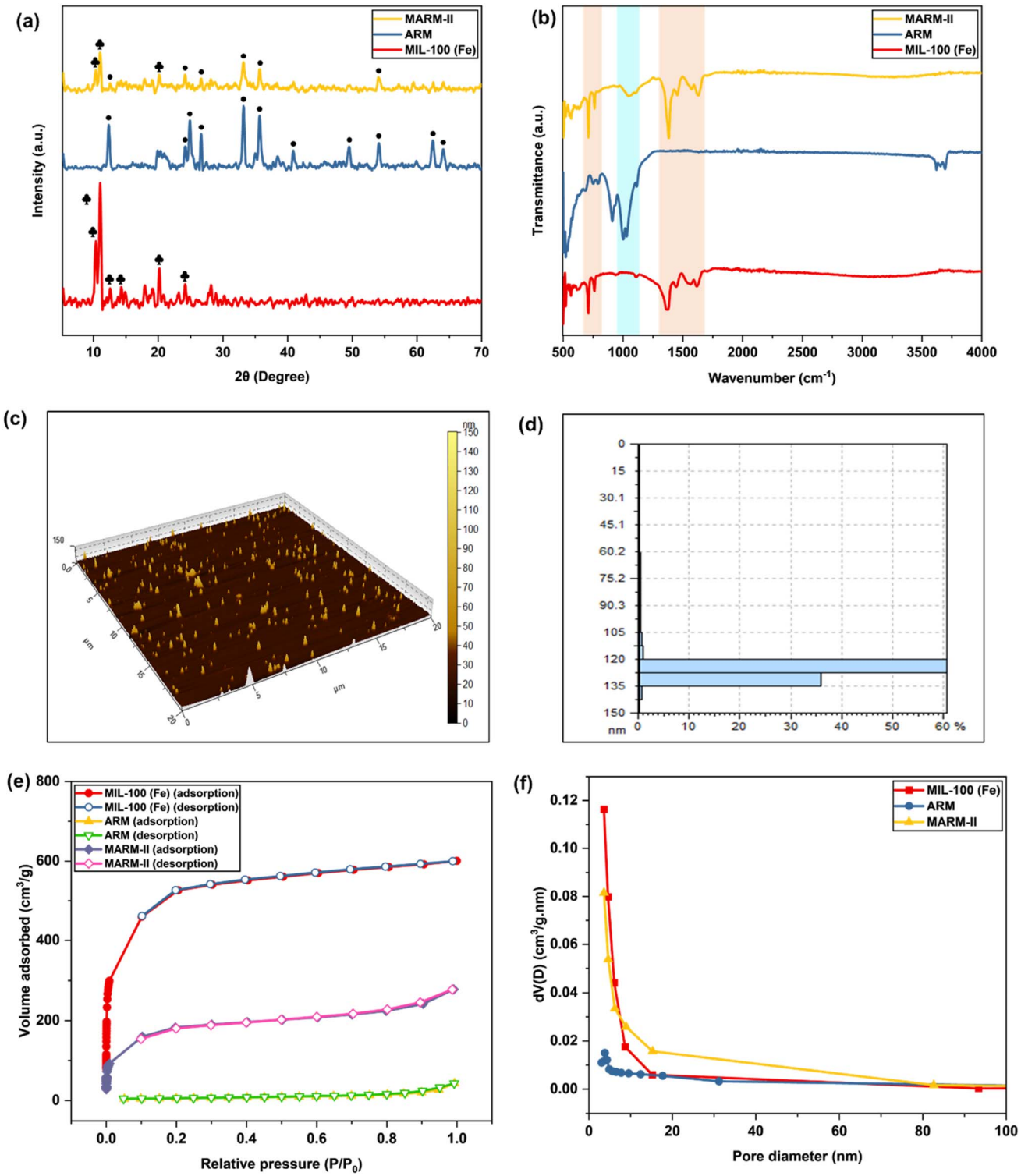

Fig. 2 (a) XRD patterns, (b) FTIR spectra, (c) surface topographical profile, (d) roughness distribution histogram, (e) N_2 adsorption–desorption isotherms, and (f) pore size distribution curves of pristine MIL-100 (Fe), ARM, and MARM-II composite.

33.18°, 35.66°, 40.88°, 49.50°, 54.11°, 62.42°, and 64.05° can be linked to the (012), (104), (110), (113), (024), (116), (214), and (300) crystal planes of the hematite phase (α-Fe_2O_3).[56,57] The standard XRD pattern of α-Fe_2O_3 (reference code – 00-033-0664) and simulated XRD pattern of MIL-100 (Fe) (CIF file no. -7102029) has been presented in Fig. S1. The As anticipated, the XRD pattern of the MARM-II composite represented peaks associated with the aforementioned constituent materials, confirming its successful synthesis.

Fourier transform infrared (FTIR) spectroscopy was deployed to determine the vibrational modes of the chemical bonds in the as-prepared pristine and composite materials. The FTIR spectrum of MIL-100 (Fe) exhibited two peaks at 710 cm^{-1} and 762 cm^{-1}, corresponding to the Fe–OH vibrations (Fig. 2b).[58] The two distinct peaks evident around 1444 cm^{-1} and 1375 cm^{-1} can be linked to the symmetric and asymmetric stretching vibrations of the O–C–O bonds in the organic ligand, respectively.[59] Moreover, the peak observed at 1617 cm^{-1} could be linked to the phenyl and carboxylate groups of trimesic acid.[60] The peak observed at 521 cm^{-1}, common in the FTIR spectra of MIL-100 (Fe) and ARM, is indicative of the Fe–O bond.[61] The peak appearing at 909 cm^{-1} in the latter spectrum corresponds to the bending vibration of Al–OH–Al bonds.[62] The asymmetric Si–O–Al and Si–O–Si stretching bands were

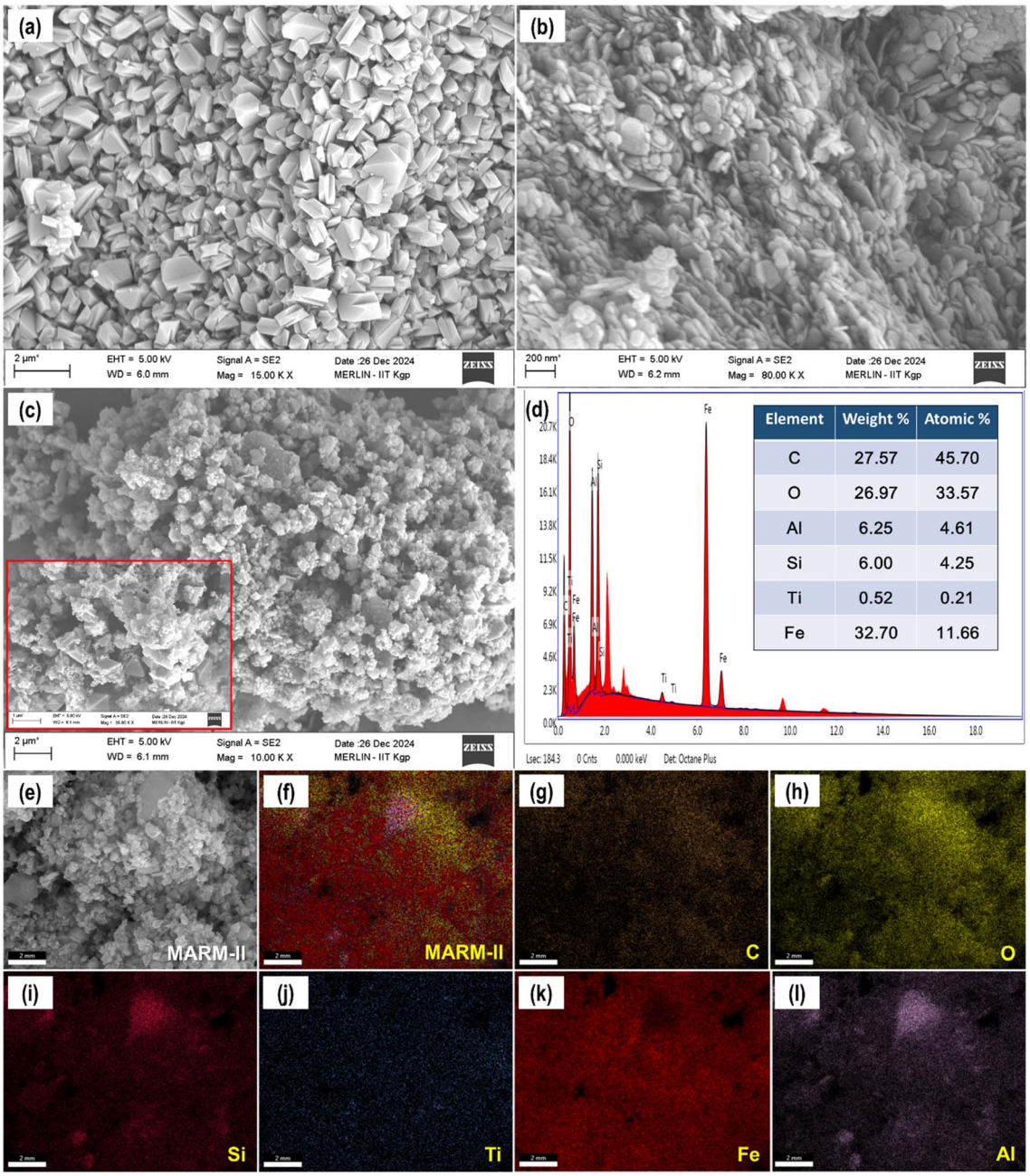

Fig. 3 FEG-SEM images of (a) MIL-100 (Fe), (b) ARM, and (c) MARM-II composite. (d) EDS spectra, and (e–l) elemental mapping of MARM-II composite.

indicated by the intense peaks appearing at 1002 cm^{-1} and 1030 cm^{-1}, respectively.[63,64] Additionally, the stretching vibrations of the –OH groups were indicated by the peaks noted at 3621 cm^{-1} and 3693 cm^{-1}.[65] The FTIR spectrum of the MARM-II composite consisted of distinctive peaks of MIL-100 (Fe) and ARM, implying effective integration of the individual components.

The surface topographical features of the MARM-II composite were evaluated utilizing atomic force microscopy (AFM). Fig. 2c illustrates that AFM imaging uncovered a heterogeneous surface, indicating the presence of surface imperfections marked by both elevations and indentations across the MARM-II composite. According to the surface height profile, most particles exhibited sizes between roughly ~105 nm and ~137 nm (Fig. 2d). In addition, other height parameters are depicted in Fig. S2.

The textural properties of the as-prepared adsorptive materials were recorded through Brunauer–Emmett–Teller (BET) and Barrett–Joyner–Halenda (BJH) analysis. Fig. 2e presents the N_2 adsorption–desorption isotherm of MIL-100 (Fe), ARM, and MARM-II. MIL-100 (Fe) displays a concave curve in association with the relative pressure (P/P_0), characteristic of a Type I isotherm, which indicates its microporous structure and high specific surface area (SSA) (1845.522 m^2 g^{-1}). The forces from opposing pore walls overlap in micropores, causing rapid filling at low relative pressures. This phenomenon is evidenced by a sharp rise at the beginning of the adsorption isotherm, followed by a plateau at higher relative pressures.[66] The N_2 sorption profile of ARM had a Type IV isotherm, indicative of mesoporous material, and exhibited an H3 hysteresis loop, often associated with plate-like particle aggregates that result in slit-shaped pores.[67] The SSA of ARM was found to be 21.339 m^2 g^{-1}. Furthermore, the MARM-II composite showed a combination of Type I and Type IV isotherms, and an H2 hysteresis loop, confirming the presence of both micropores and mesopores,[68] with a SSA of 651.741 m^2 g^{-1}. Reportedly, the presence of micropores in adsorbents facilitates the selective adsorption of small-sized adsorbates,[69,70] whereas mesopores accommodate relatively larger molecules and enhance mass transfer.[70–72] The BJH pore size distribution plots for MIL-100 (Fe), ARM, and MARM-II are presented in Fig. 2f, with details of corresponding pore sizes and volumes in Table S3.

The morphological features of the as-synthesized adsorptive materials were determined by field emission gun scanning electron microscopy (FEGSEM) and high-resolution transmission electron microscopy (HR-TEM). As depicted in Fig. 3a, pristine MIL-100 (Fe) displays a morphology that slightly deviates from the typical bipyramidal octahedral shape, instead

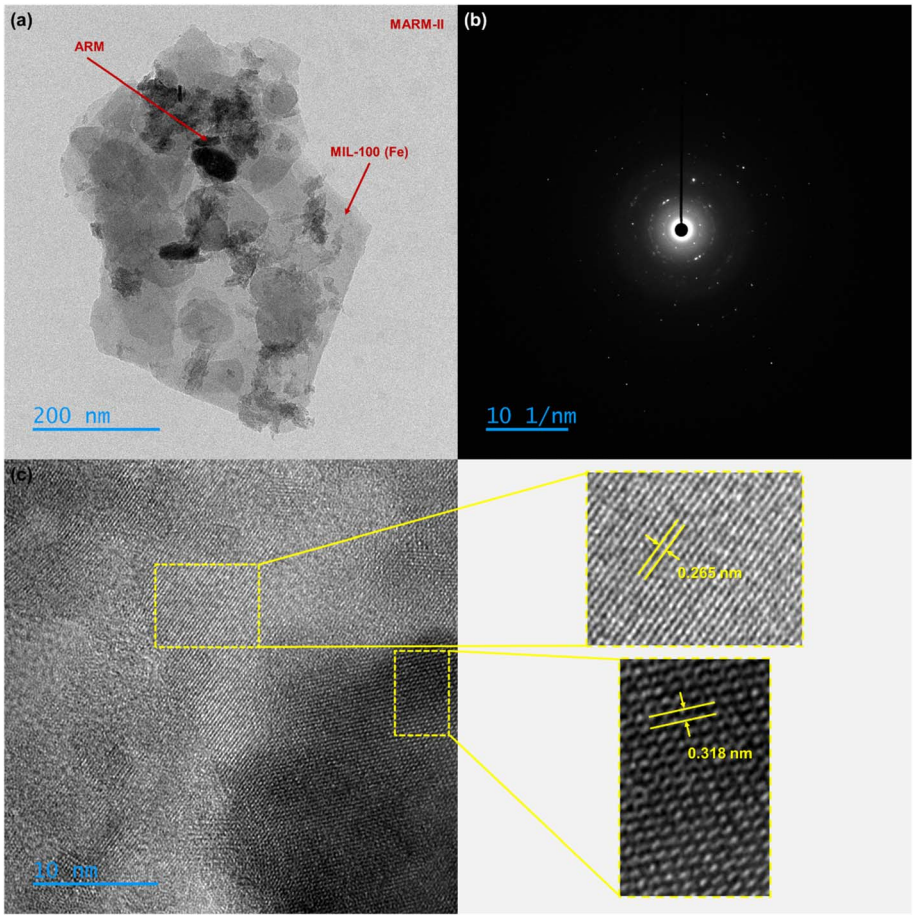

Fig. 4 (a) TEM image, (b) SAED pattern, (c) HR-TEM image of MARM-II composite (inset selected area showcasing lattice spacings).

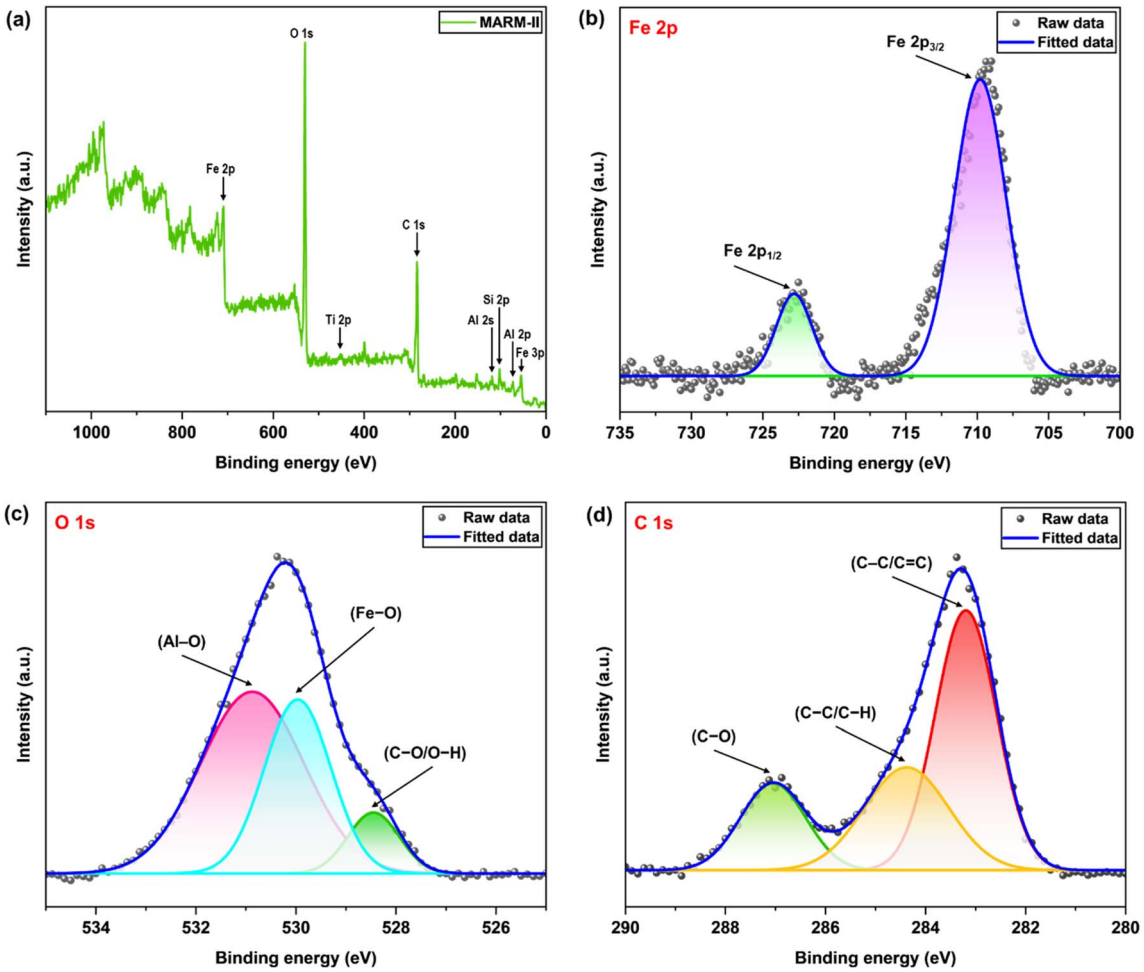

Fig. 5 (a) XPS survey scan of MARM-II composite, and high resolution XPS spectrum of (b) Fe 2p, (c) O 1s, and (d) C 1s.

consisting of irregularly shaped crystals with non-uniform sizes. This can be attributed either to the Fe(BTC) phase or to MIL-100 (Fe) crystals that have still not developed into bipyramids.[73] The ARM sample displayed a plate-like morphology (Fig. 3b), which aligns with the findings of the N_2 adsorption–desorption analysis and is consistent with existing literature.[74] In the context of MARM-II, the observed morphology revealed lamellar ARM particles dispersed over bipyramidal octahedral-shaped MIL-100 (Fe) crystals (Fig. 3c). Moreover, the energy-dispersive X-ray spectroscopy (EDS) spectrum (Fig. 3d), along with the corresponding elemental maps (Fig. 3e–l), confirms the co-occurrence and uniform distribution of C, O, Si, Ti, Fe, and Al within the MARM-II composite. The morphological configuration of pristine ARM and MIL-100 (Fe) within the MARM-II composite was reaffirmed by TEM imaging, as illustrated in Fig. 4a. The selected area electron diffraction (SAED) pattern, characterized by concentric rings and bright spots, indicates the polycrystalline nature of the MARM-II composite (Fig. 4b). As shown in Fig. 4c, the HR-TEM imaging of MARM-II displayed two distinct interplanar spacings of 0.265 nm and 0.318 nm, which could be associated with the (104) plane of α-Fe_2O_3,[75] and (002) plane of sp^2 hybridized graphitic carbon.[76]

X-ray photoelectron spectroscopy (XPS) was deployed to assess the surface chemical state and elemental composition of MARM-II. As depicted in Fig. 5a, the survey profile indicated the co-existence of various elements, including Fe, O, C, Al, Ti, and Si in MARM-II,[77] with pronounced peaks for Fe, O, and C signifying their predominance in the composition. In the high-resolution spectrum of Fe 2p (Fig. 5b), the peaks observed at 722.82 eV and 709.81 eV are linked to Fe $2p_{1/2}$ and Fe $2p_{3/2}$, respectively.[78] The O 1s spectrum can be deconvoluted into three peaks located at 530.87 eV, 529.96 eV, and 528.44 eV (Fig. 5c). The two major peaks observed at binding energies of 530.87 eV and 529.96 eV were ascribed to metal–oxygen bonds, associated with Al–O and Fe–O bonds, respectively.[79,80] Moreover, the peak at 528.44 eV could be associated with the C–O/O–H species.[81] Furthermore, the high-resolution spectrum of C 1s exhibited three peaks located at 287.06 eV, 284.37 eV, and 283.18 eV, which can be linked to C–O, C–C/C–H, and C–C/C=C species, respectively (Fig. 5d).[82–84]

The thermal stability of the MARM-II composite was determined through thermogravimetric analysis (TGA). As illustrated in Fig. S3, the initial decrease in weight below ~60 °C corresponds to the release of water molecules trapped in the

material's pores. Thereafter, weight loss occurring between ~60 °C and ~300 °C relates to the loss of water molecules complexed with the iron trimer clusters present within the MIL-100 (Fe).[85] The sudden weight loss of ~35% noted in the temperature range ~300–390 °C in the TGA profile of MARM-II is assigned mainly to the disintegration of linkers inside the MIL-100 (Fe) framework.[86] Any further weight loss in the temperature range of ~390–800 °C could likely be associated with the oxidation of the residual linkers of MIL-100 (Fe) in MARM-II. The aforementioned weight loss may also be slightly contributed to the release of CO_2 resulting from the thermal decomposition of $CaCO_3$ to CaO in the ARM portion of the MARM-II composite.[87] In the differential thermal analysis (DTA) plot of MARM-II, an exothermic peak was observed at ~386 °C.[88]

3.2. Adsorptive removal of organic pollutants

3.2.1. Effect of contact time and initial pollutant concentration. The contact time between adsorbate and adsorbent is a critical factor in the adsorption process. The rapid adsorption of the organic pollutants and the attainment of near equilibrium conditions within a timeframe demonstrate the effectiveness and appropriateness of the adsorbent. The impact of contact time on LVX, MLB, and CNR elimination utilizing MARM-II was evaluated by changing contact time from 15 to 120 min, keeping other parameters constant (initial LVX, MLB, and CNR concentration: 10 mg L^{-1} each, MARM-II dose: 0.4 g L^{-1}, solution pH: 7, and temperature: 27 ± 3 °C). Fig. 6a illustrates the percentage removal of LVX, MLB, and CNR using MARM-II with respect to time. After 60 min, the removal efficiencies achieved using MARM-II were 95.864 ± 1.286% for LVX, 92.923 ± 1.519% for MLB, and 86.506 ± 1.208% for CNR, respectively. The rapid adsorption of the investigated organic pollutants at the initial stage was ascribed to the availability of abundant active sites on the MARM-II surface. Furthermore, the removal efficiencies for LVX, MLB, and CNR showed no significant increase beyond a certain contact time, indicating the saturation of available adsorptive sites on the MARM-II surface and the attainment of adsorption equilibrium. The equilibrium was reached at 105 min for CNR and at 60 min for both LVX and MLB, with no significant changes in removal efficiencies beyond these points. Initially, abundant vacant surface sites enabled rapid adsorption, but over time, repulsive forces between adsorbed and bulk-phase solute molecules hindered further uptake.[89] The adsorptive removal of the aforementioned pollutants using pristine ARM, MIL-100 (Fe), and other MARM variants is given in Fig. S4. Furthermore, Table S4 compares the removal performance of MARM-II composite for LVX (96.102 ± 0.997%), MLB (93.077 ± 0.593%), and CNR (89.739 ± 1.119%) with that of other adsorbents previously reported. As mentioned in Table S4, the adsorptive performance of MARM-II is on par with several other reported Fe-based adsorbents, despite operating at relatively moderate initial pollutant concentrations and neutral pH conditions. Unlike many high-capacity adsorbents that rely on toxic solvents, extreme synthesis conditions (high

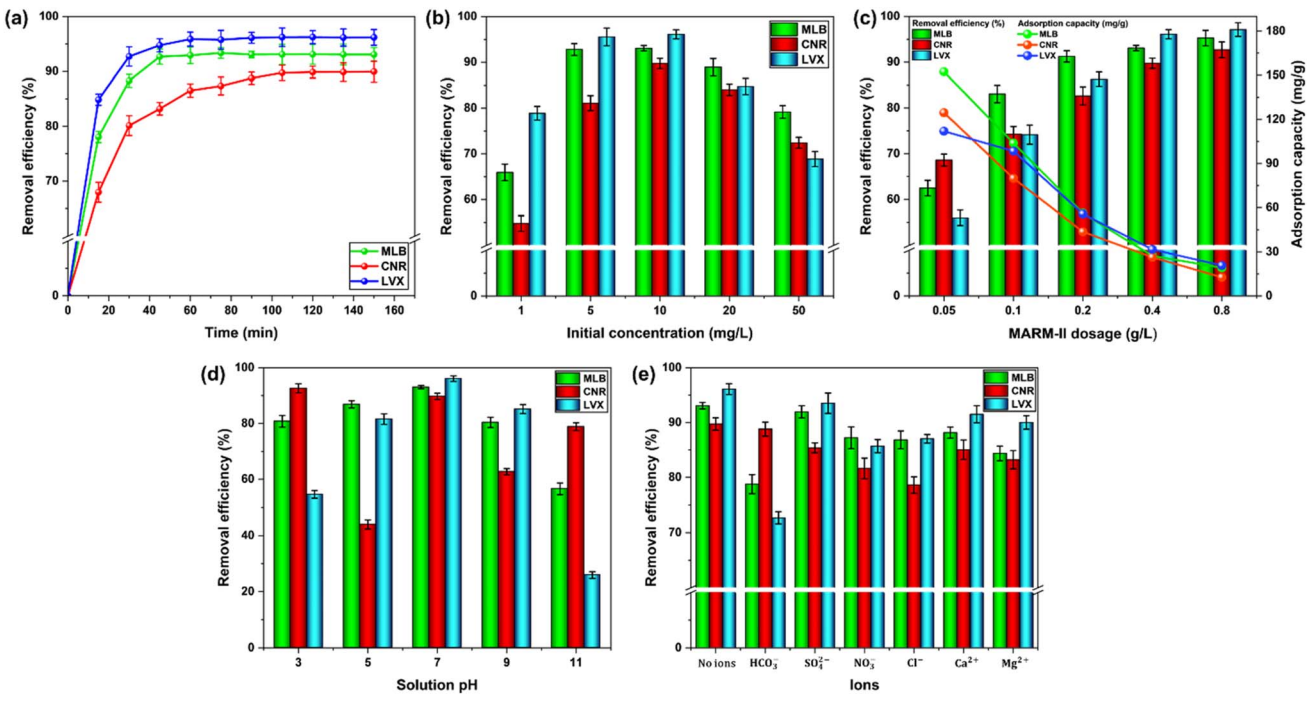

Fig. 6 (a) Effect of contact time (initial MLB, CNR, and LVX concentration: 10 mg L^{-1} each, MARM-II dose: 0.4 g L^{-1}, solution pH: 7, and temperature: 27 ± 3 °C), (b) initial concentration (contact time: 150 min, MARM-II dose: 0.4 g L^{-1}, solution pH: 7, and temperature: 27 ± 3 °C), (c) MARM-II dosage (initial MLB, CNR, and LVX concentration: 10 mg L^{-1} each, contact time: 150 min, solution pH: 7, and temperature: 27 ± 3 °C), (d) solution pH (initial MLB, CNR, and LVX concentration: 10 mg L^{-1} each, contact time: 150 min, MARM-II dose: 0.4 g L^{-1}, and temperature: 27 ± 3 °C), and (e) inorganic ions (contact time: 150 min, initial MLB, CNR, and LVX concentration: 10 mg L^{-1} each, MARM-II dose: 0.4 g L^{-1}, solution pH: 7, and temperature: 27 ± 3 °C).

temperature and pressure), MARM-II is prepared employing a simple co-precipitation technique using low-cost and industrial waste-derived activated red mud, combined with MIL-100 (Fe). This approach not only promotes sustainability but also confirms environmental relevance. The MARM-II composite exhibits significant adsorption capacities for both dyes (MLB, CNR) and an antibiotic (LVX), indicating its effectiveness in removing these pollutants.

The effect of the initial concentrations of LVX, MLB, and CNR on their removal utilizing MARM-II was investigated by adjusting the pollutant concentration from 1 mg L^{-1} to 50 mg L^{-1} while maintaining a constant adsorbent dosage of 0.4 g L^{-1} and a solution pH of 7. As depicted in Fig. 6b, at first, when the initial concentrations of LVX, MLB, and CNR were raised from 1 mg L^{-1} to 10 mg L^{-1}, the removal efficiencies increased by ~17%, ~27%, and ~34%, respectively. It can be supported by the rationale that the initial number of pollutant molecules on the exposed surface area of the MARM-II composite is minimal at lower concentrations.[90] However, when the initial concentrations of LVX, MLB, and CNR were increased from 10 mg L^{-1} to 50 mg L^{-1}, their respective removal efficiencies decreased from 96.102 ± 0.997%, 93.077 ± 0.593%, and 89.739 ± 1.119% to 68.858 ± 1.648%, 79.173 ± 1.383%, and 72.426 ± 1.186±%, due to the fewer number of adsorptive sites in comparison to the number of pollutant molecules at higher concentrations.[90]

3.2.2. Effect of adsorbent dosage. The MARM-II dosages were altered from 0.05 g L^{-1} to 0.8 g L^{-1} to assess its impact on the removal of LVX, MLB, and CNR, keeping other parameters constant (initial LVX, MLB, and CNR concentration: 10 mg L^{-1} each, solution pH: 7, and temperature: 27 ± 3 °C). As displayed in Fig. 6c, the experimental findings showed that the percentage removal of LVX, MLB, and CNR enhances progressively with an increase in MARM-II dosage. This could be linked to the augmented number of adsorptive sites with the rise in adsorbent dosage.[89] Beyond a MARM-II dose of 0.4 g L^{-1}, no notable improvement in the removal efficiencies of the organic pollutants was observed. Accordingly, 0.4 g L^{-1} was determined to be the optimum dosage for further experiments. Although the overall removal efficiencies of LVX, MLB, and CNR increased with higher adsorbent dosage, the uptakes per gram of adsorbent declined. This reduction can be ascribed to the saturation of adsorptive sites, where increasing the adsorbent dose leaves many sites underutilized, resulting in a reduced adsorption capacity.[91]

3.2.3. Effect of solution pH. The solution pH influences electrostatic interactions, the ionization state of adsorbates, and the surface charge of the adsorbent, thereby regulating the adsorptive removal of organic pollutants. Thus, the effect of solution pH on adsorptive removal becomes necessary (Fig. 6d). Reportedly, CNR is an anionic dye, characterized by multiple sulphonic groups (–SO_3–H) within its chemical structure. These groups dissociate in aqueous solutions, resulting in the formation of a negatively charged sulfonate group (–SO_3^-).[17] The presence of these negatively charged groups classifies CNR as an anionic dye, indicating that it possesses a net negative charge. Zeta-potential analysis of MARM-II demonstrated the point of zero charge (pH_{ZPC}) to be located at pH 6.35, as depicted in Fig. S5, imparting it a positive charge below this point. Thus, the aforementioned opposite charges render a high removal efficiency of 92.643 ± 1.602% at pH 3, which then reduces to 43.972 ± 1.793% as the solution pH is increased to 5. Moreover, the carboxylate groups (–COO^-) of MIL-100 (Fe) could form hydrogen bonds with the amino (–NH_2) groups of CNR, while π–π interaction between the aromatic moieties of the MOF and CNR further stabilizes adsorption.[92] Although electrostatic repulsion between the negatively charged MARM-II surface and the –SO_3^- group would normally hinder adsorption, the aforementioned secondary interactions could promote the adsorptive removal of CNR at the neutral pH.[93–95] When the solution pH rose from 7 to 9, the CNR removal further dropped. This decline can be assigned to electrostatic repulsion between the increasingly negative surface charge of the MARM-II composite and the –SO_3^- groups of CNR. However, at a strongly alkaline condition (pH 11), a slight increase in removal efficiency was observed compared to pH 9. This improvement can be ascribed to the chemisorption of CNR molecules onto the open Fe sites of the MIL-100 (Fe) component within the MARM-II composite,[96] which overcomes the unfavorable electrostatic repulsion.

In contrast, MLB is a cationic phenothiazine dye that exists as a positively charged species, with its positive charge delocalized across the aromatic ring system, primarily on methylated nitrogen groups.[97] Reportedly, MLB can exist in aqueous solution as either a cationic species (MLB^+) or an undissociated neutral molecule (MLB^0); at pH 3, MLB^0 predominates (~86%); at pH equal to its pK_a (3.8), both MLB^0 and MLB^+ co-exist in nearly equal proportions (~50% each); and at pH values above 6, MLB is present primarily as MLB^+.[98] Under acidic conditions (pH 3), the adsorption of MLB is comparatively lower than that observed at pH 5 and 7. This is ascribed to the high concentration of H^+ ions in the acidic environment, which inhibits the ionization of MLB molecules to some degree, thereby diminishing the adsorption efficiency.[99] At neutral pH, the MARM-II surface carries a slight negative charge, which promotes electrostatic attraction with the MLB^+ species, thereby resulting in maximum removal efficiency. Furthermore, under alkaline conditions (pH 9 and 11), excess OH^- ions in solution electrostatically stabilize MLB^+, making it preferentially remain solvated rather than adsorbed onto the negatively charged MARM-II surface.[99]

In the context of LVX, the relationship between the removal efficiency and the solution pH can be elucidated based on electrostatic interactions between the LVX molecules and the positively/negatively charged surface of MARM-II. The LVX molecule exhibits two characteristic dissociation constants (pK_{a1} = 5.59 and pK_{a2} = 7.94),[100] which regulate its ionization behavior, and result in the predominance of three species under different pH conditions: the protonated form (LVX^+), the zwitterionic form (LVX±), and the monoanionic form (LVX^-). At pH 3, the positively charged surface of MARM-II likely repels LVX^+ species, resulting in a significantly low removal efficiency of 54.713 ± 1.348%. As the solution pH increased to 5, this electrostatic repulsion weakened, and the removal efficiency

gradually improved, reaching around 82%. At neutral pH, LVX predominantly existed in LVX± form, where the protonated –NH_2^+ group interacted favorably with the slightly negatively charged MARM-II surface, and likely led to maximum LVX adsorption. Furthermore, at more alkaline pH values, increasingly negative charge of the MARM-II surface induces strong electrostatic repulsion to the LVX^- species, thereby reducing removal efficiency. Overall, at neutral pH, the simultaneous removal of MLB, CNR, and LVX was maximum; therefore, it was selected as the optimum for subsequent studies.

3.2.4. Effect of inorganic ions. The co-existence of inorganic ions in real water matrices can hinder the absorptive removal of targeted pollutants; therefore, their influence on the adsorption of a mixture of MLB, CNR, and LVX was systematically investigated, and findings are depicted in (Fig. 6e). In a typical experimental procedure, representative anions (Cl^-, SO_4^{2-}, HCO_3^-, and NO_3^-), and cations (Ca^{2+}, and Mg^{2+}) were introduced in the adsorbent–adsorbate system, each at a concentration of 100 mg L^{-1}. As previously reported, Cl^-, SO_4^{2-}, NO_3^-, Mg^{2+}, and Ca^{2+} showcased minimal inhibitory effects on adsorption,[19,101,102] and similar observations were made in the present study. In contrast, HCO_3^-, which tends to dissociate into CO_3^{2-} with high negative charge density; it could readily occupy the adsorptive sites on the adsorbent surface,[101] thereby adversely impacting the uptake of MLB, CNR, and LVX. To further extend the discussion of the inhibitory interaction of HCO_3^-/CO_3^{2-} with the MARM-II adsorbent, it has been shown that these species form complexes on the surface of the Fe-based adsorbents through interactions, showing their direct participation in surface binding competition.[103] Moreover, the synergistic inhibitory effects of HCO_3^-/CO_3^{2-} on Fe-oxides (herein identified as the dominant phase by XRD) have been reported to negatively affect the adsorption kinetics of organic pollutants.[104]

3.2.5. Effect of real wastewater matrix. The effect of the real wastewater matrix was investigated to evaluate its influence on the adsorption of MLB, CNR, and LVX onto the MARM-II surface. Table S5 presents the characteristics of the secondary wastewater used in the present study. A mixture of the aforementioned pollutants was introduced into the secondary wastewater, each having an initial concentration of 10 mg L^{-1}. A reduction in the adsorption efficiency of MARM-II was observed for MLB, CNR, and LVX, with decline of ~9%, ~14%, and ~11%, respectively, as shown in Fig. S6. This decline in adsorption efficiency can be attributed to the presence of interfering constituents in the real wastewater matrix, including turbidity, suspended solids (SS), inorganic ions, and organic matter, which may compete with MLB, CNR, and LVX molecules for the available active adsorptive sites on the MARM-II surface. SS present in wastewater interferes with the adsorption of organic pollutants, limiting both adsorption capacity and rate because of competitive interactions with the adsorbent surface.[105] In addition, the presence of dissolved ions, reflected in TDS, increases the ionic strength of the solution, which could alter electrostatic interactions and influence the adsorptive behavior of organic pollutants on the adsorbent surface.[106] The presence of anions, particularly HCO_3^-/CO_3^{2-} (as discussed in Section 3.2.4) could compete for adsorptive sites, thereby limiting MLB, CNR, and LVX adsorption on the MARM-II surface. Furthermore, residual COD/TOC in WWTP effluent indicates the presence of dissolved organic matter (DOM), which reportedly interacts with adsorbent surfaces, thereby negatively affecting organic pollutant removal through adsorptive site competition and surface interactions.[107]

3.3. Adsorption kinetics study

Adsorption kinetics pertains to the rate and mechanism by which pollutants transition from the solution phase to the surface of the adsorbent. Kinetic models aid in determining whether the process is regulated by surface reactions, pore diffusion, or a combination of both. The findings of the kinetics study are displayed in Fig. 7a–d, with the corresponding parameters summarized in Table S6. The kinetic study showcased that both PFO and PSO kinetic models exhibited excellent fitting ($R^2 > 0.99$) for the adsorption of MLB, CNR, and LVX onto MARM-II composite. The fit to the PSO kinetic model showed the possibility that chemisorption, comprising valence forces through electron sharing or exchange,[108] might play a primary role in the adsorptive removal of the aforementioned pollutants. However, the calculated enthalpy values for MLB (−32.47 kJ mol^{-1}), CNR (−22.43 kJ mol^{-1}), and LVX (−60.04 kJ mol^{-1}) in Section 3.5, are notably lower than the chemisorption range (80–240 kJ mol^{-1})[109] typically linked with the chemical bond formation. Therefore, the adsorption mechanism for MLB and CNR, showcasing low enthalpy values, is consistent with physisorption. On the contrary, the higher enthalpy value noted for LVX implies borderline between strong physisorption and weak chemisorption.[110] The pollutant-specific kinetics indicated that LVX demonstrated rapid adsorption, characterized by the highest rate constants in both PFO (k_1 = 0.1421 min^{-1}) and PSO (k_2 = 0.0140 g mg^{-1}. min), which signifies a strong affinity and swift uptake. MLB showed slightly lower rate constants (k_1 = 0.1192 min^{-1}, k_2 = 0.0113 g mg^{-1}. min), whereas CNR demonstrated the slowest kinetics (k_1 = 0.0914 min^{-1}; k_2 = 0.0065 g mg^{-1} min^{-1}). The rationale for this observation is that existing adsorptive sites become increasingly shielded by previously adsorbed dye or restricted by steric hindrance, leading to a reduced adsorption rate.[111]

The Elovich kinetic model further delved into the heterogeneous nature of the MARM-II surface. The α value was significantly high for MLB (3.26×10^5 mg g^{-1} min^{-1}) and LVX (9.37×10^7 mg g^{-1} min^{-1}), implying rapid coverage of adsorptive sites during the initial stage of the adsorption process.[112] Contrastingly, CNR displayed a notably lower α value (497.88 mg g^{-1} min^{-1}), indicating its slower uptake and weaker interaction with the active sites on the MARM-II surface. Moreover, β, which correspond to the extent of surface coverage and the change in activation energy during chemisorption,[113] was lowest for CNR. This indicates a gradual increase in activation energy as adsorption proceeds, resulting in a slower decline in adsorption rate. The IPD model highlights a multi-stage adsorption mechanism marked by an initial rapid uptake (Stage I), followed by a slower intraparticle diffusion phase (Stage II), and

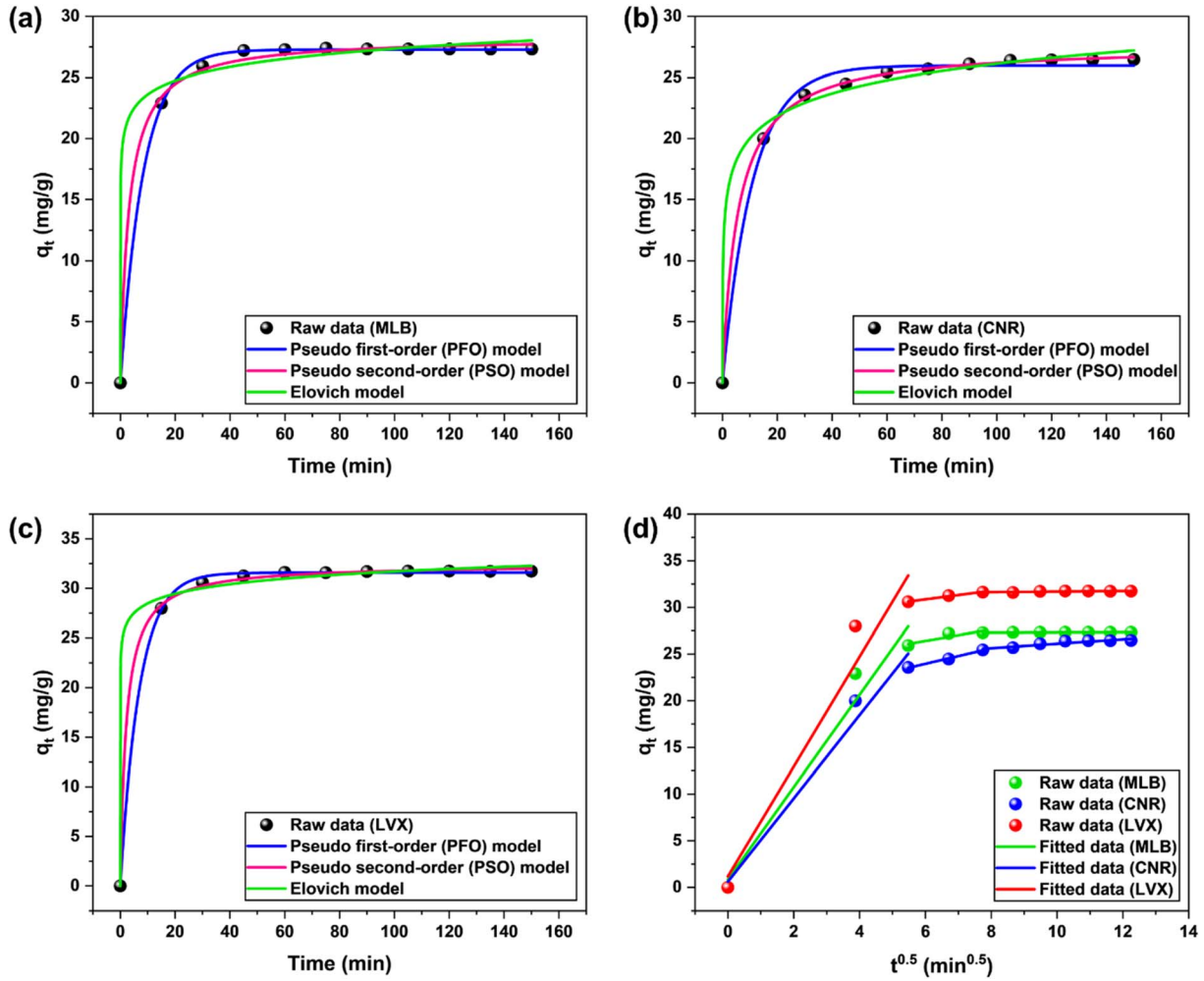

Fig. 7 Fitting of the experimental adsorption data to the PFO, PSO, and Elovich kinetic models for (a) MLB, (b) CNR, and (c) LVX onto the MARM-II composite. (d) Kinetic data fitted to the intraparticle diffusion model for the adsorption of MLB, CNR, and LVX onto the MARM-II composite.

concluding with a final equilibrium plateau (Stage III). The plots for MLB, CNR, and LVX did not exactly pass through the origin, implying that the intraparticle diffusion was not the only rate-limiting step.[114] Overall, the aforementioned results establish that MLB, CNR, and LVX adsorption onto the MARM-II composite is governed mainly by physisorption with rapid initial uptake, followed by slow diffusion into pores and adsorptive site saturation.

3.4. Adsorption isotherms study

To better understand the equilibrium mechanism of MLB, CNR, and LVX adsorption onto the MARM-II composite, the experimental data were fitted to Langmuir, Freundlich, Sips, and Redlich–Peterson isotherms. The findings of the adsorption isotherms study are presented in Fig. 8a–c, and the related parameters are mentioned in Table S7. In the context of the Langmuir isotherm, adsorption occurs through chemical binding at a finite number of well-defined sites, ultimately leading to the formation of a saturated monolayer on the adsorbent surface.[115] The fitted parameters showed Q_{max} to be 123.021 ± 11.9261 mg g^{-1}, 143.934 ± 24.248 mg g^{-1}, 97.657 ± 5.686 mg g^{-1} for MLB, CNR, and LVX, respectively, which indicated a strong affinity of the MARM-II composite towards the aforementioned pollutants. The higher Q_{max} value for CNR in comparison to others can be ascribed to the –SO_3^- and –NH_2 groups, which strengthen electrostatic attraction, H-bonding, respectively, alongside its aromatic structure that facilitates π–π interactions with the adsorbent surface.[92]

While the Langmuir isotherm for CNR showcased a satisfactory fit with R^2 ranging between 0.963–0.977, the comparatively high χ^2 value (~38.622) indicated marginal deviations from ideal monolayer adsorption. Furthermore, the Freundlich isotherm (Fig. 8d–f), representative of multilayer adsorption on a heterogeneous surface,[115] displayed $n > 1$ for all pollutants (2.454 for LVX, 1.784 for MLB, and 1.539 for CNR), confirming favorable adsorption. Notably, the Freundlich fits displayed R^2 values ranging from 0.939 to 0.968, lower than those obtained from the Langmuir isotherm (0.973–0.992). This shows that the adsorption of LVX, CNR, and MLB occurs heterogeneously on the MARM-II surface, but the Freundlich isotherm cannot solely depict the equilibrium behavior of the system.

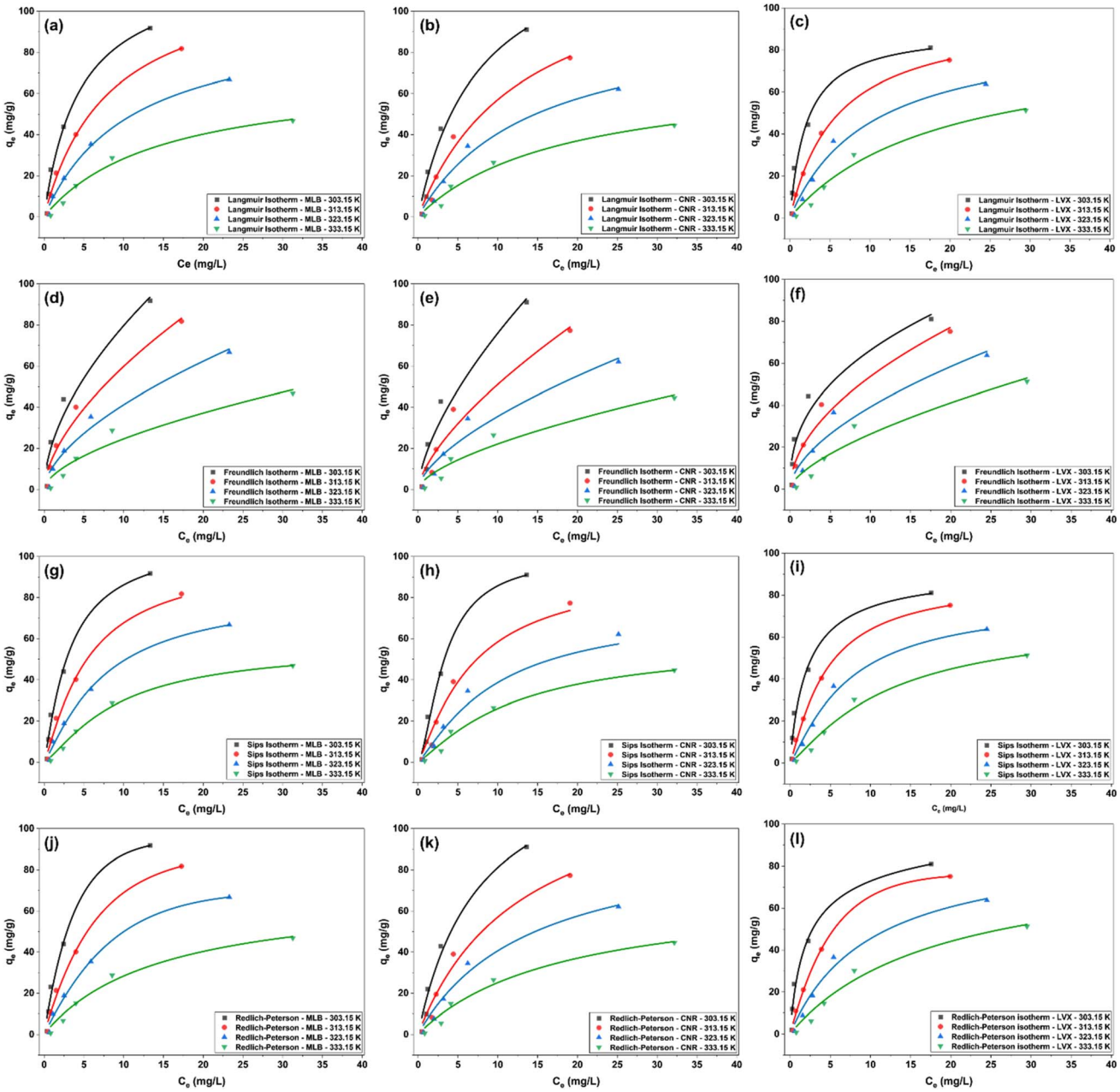

Fig. 8 Fitting of the experimental adsorption data in Langmuir isotherm for (a) MLB, (b) CNR, and (c) LVX; Freundlich isotherm for (d) MLB, (e) CNR, and (f) LVX; Sips isotherm for (g) MLB, (h) CNR, and (i) LVX; and Redlich–Peterson isotherm for (j) MLB, (k) CNR, and (l) LVX onto the MARM-II composite.

The Sips isotherm (Fig. 8g–i), comprising attributes of both Langmuir and Freundlich isotherms, displayed the best fit, with the lower χ^2, compared to other models. For LVX ($m = 0.941$) and MLB ($m = 1.185$), the value of m approaches 1, suggesting that the adsorption behavior approximates the Langmuir model defined by monolayer adsorption. On the contrary, a higher m value for CNR ($m = 1.589$) indicates stronger heterogeneity effects, possibly attributed to steric hindrance from its bulky molecular structure, which restricts adsorptive site accessibility.[116] Likewise, the Redlich–Peterson isotherm (Fig. 8j–l), which integrates aspects of both the Langmuir and the Freundlich isotherms, demonstrated satisfactory fits ($R^2 =$ 0.94–0.996 for LVX; 0.978–0.992 for MLB; 0.973–0.977 for CNR), thereby validating the aforementioned finding.

3.5. Adsorption thermodynamics study

The thermodynamics study was conducted to evaluate the spontaneity and exothermic/endothermic nature of the adsorption of MLB, CNR, and LVX onto the MARM-II composite. The findings of the thermodynamics study are depicted in Fig. S7 and the associated parameters mentioned in Table S8. The negative $\Delta G°$ values for the aforementioned

pollutants, in conjunction with rising temperature, suggest that the adsorptive process is spontaneous.[117] The negative ΔH° values reveal the exothermic nature of MLB, CNR, and LVX adsorption.[118] Moreover, the negative ΔS° values for MLB and LVX signify increased orderliness at the adsorbent–adsorbate interface due to strong binding of the pollutants on the MARM-II surface.[119,120] The slightly positive ΔS° value noted for CNR indicated an increase in randomness at the adsorbate–adsorbent interface possibly due to the partial desolvation effects during adsorption process.[121] The Van't Hoff analysis's dependability is shown by the R^2 values (0.913–0.981), thus explaining almost all variability in the observed data.

3.6. Adsorptive mechanisms for MLB, CNR, and LVX

The mechanistic insights governing the adsorptive removal of LVX, MLB, and CNR using the MARM-II composite arise from the combined effects of their functional groups, the pH-dependent speciation of the aforementioned pollutants, and the surface chemistry of the MARM-II composite (Fig. 9). The mechanistic insights regarding MLB, CNR, and LVX adsorption onto the MARM-II surface have been elaborately covered in Section 3.2.3 and summarized in the present section. The LVX molecule primarily exists as LVX± species, depending on its pK_a values, where positively charged $-NH_2^+$ group exhibits strong electrostatic affinity toward the slightly negative surface of MARM-II (pH_{ZPC} located at pH 6.35), ensuring its maximum removal. CNR was effectively adsorbed onto the MARM-II surface at multiple pH conditions, attributed to the functional groups, electrostatic attraction, and chemisorption.

Under acidic conditions, the negatively charged $-SO_3^-$ groups of CNR exhibit strong electrostatic attraction toward the positively charged surface of MARM-II, thereby enhancing its removal efficiency. At neutral pH, the hydrogen bonding between the $-COO^-$ groups on MIL-100 (Fe) and the $-NH_2$ groups of CNR, alongside π–π interactions between the aromatic moieties of the adsorbent and adsorbate, overcome the mild electrostatic repulsion, promoting CNR adsorption. The chemisorption of CNR molecules onto the open Fe sites of the MIL-100 (Fe) component within the MARM-II composite contributes to the observed adsorption at alkaline pH. Furthermore, the electrostatic attraction governed the adsorption mechanism for MLB removal, as the slightly negatively charged surface of MARM-II causes interaction with the MLB^+ species, leading to maximum removal at neutral pH.

As previously reported in multi-contaminant systems, adsorption capacities/removal efficiencies in binary and ternary mixtures often differ from those observed in single-adsorbate systems due to competitive interactions among co-existing contaminants.[122–124] Such differences arise primarily from (i) competition for the same number of active adsorption sites, and surface coverage and pore blocking by co-adsorbates,[124] (ii) antagonistic effects influenced by solution pH and resulting electrostatic interactions,[123] and (iii) differences in molecular affinity and strength of non-covalent interactions (π–π

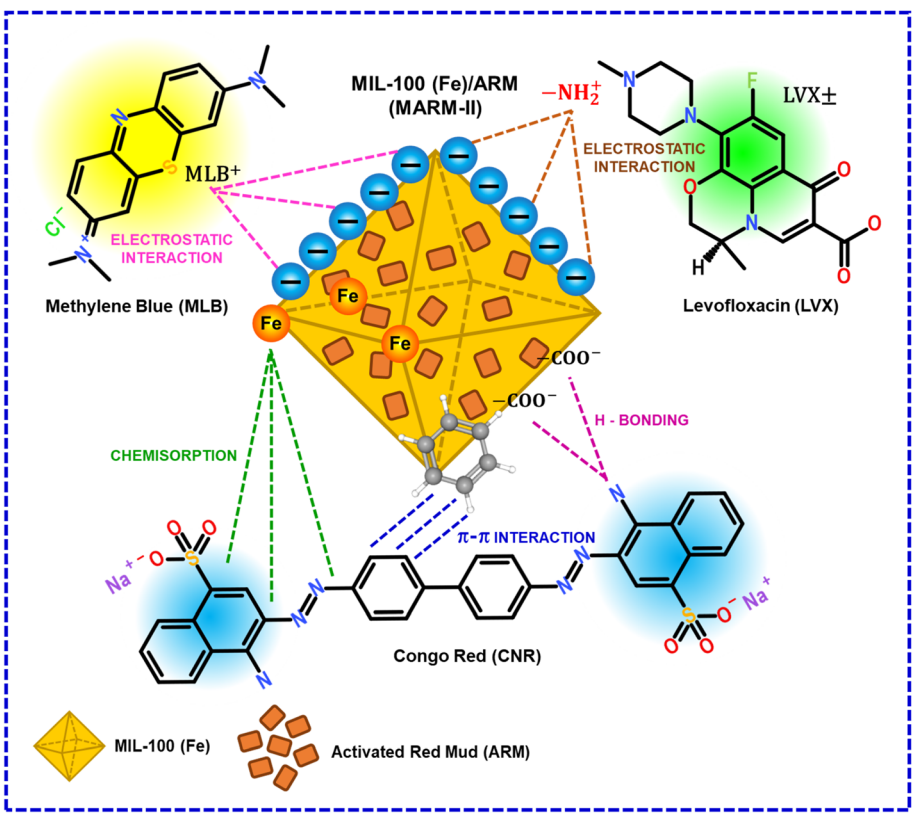

Fig. 9 Possible mechanism for the adsorption of MLB, CNR, and LVX onto the MARM-II composite.

interactions, H-bonding).[122] In the present study, applying these established observations to our MLB-CNR-LVX system on the MARM-II surface (pH_{ZPC} ~ 6.35), the selectivity trend (LVX > MLB > CNR) is consistent with a competitive scenario where LVX can access multiple interaction pathways (π–π interactions, H-bonding, and coordination to Fe sites), allowing it to outcompete dyes, while MLB is favored over CNR under near-neutral conditions due to stronger attraction to the slightly negative surface and faster uptake. Whereas, CNR is more easily suppressed in the mixture because it experiences less favorable electrostatic attraction and competes for the same number of active adsorptive sites, leading to reduced accessibility in the presence of higher-affinity species.

3.7. Desorption and reusability study

The regenerative potential and possible reuse of MARM-II composite for the adsorptive removal of MLB, CNR, and LVX were assessed through the reusability study. MARM-II composite showed a marginal drop in removal efficiency when tested up to five consecutive cycles. Following each cycle, 0.5 M HCl, 0.5 M NaOH, and acetone were used in a predefined order to regenerate the adsorptive sites on the MARM-II composite. After the fifth cycle, the MLB, CNR, and LVX removal was found to be ~79%, ~74%, and ~83%, respectively (Fig. S8). The decrease in removal efficiencies can be linked to the saturation of adsorptive sites due to the incomplete desorption of organic pollutants,[94] and the structural disintegration of the MARM-II composite[19] after several washes and drying. The diffractogram and FTIR spectrum of MARM-II composite have been presented in Fig. 10a and b, depicting differences in comparison to the pristine material. Additionally, ICP-MS analysis indicated that the concentration of Fe leached in the treated solution was negligible (~0.054 mg L^{-1}), much lower than the acceptable limit of Fe in the drinking water (0.3 mg L^{-1}),[125] thereby confirming the chemical stability of the MARM-II composite. The leached amounts of the other two primary elements,[37] *i.e.*, Al (~0.013 mg L^{-1}) and Ti (~0.071 × 10^{-3} mg L^{-1}), were also insignificant. The possibility of organic linker leaching from the MARM-II composite was investigated as a control study. The optimal dosage of MARM-II was added to a beaker containing 100 mL of DI water and stirred for the specified contact time. The aliquot was then centrifuged, and the total organic carbon (TOC) of the supernatant was measured. The TOC of the supernatant was found to be in close agreement with that of the DI water used in the study, indicating negligible leaching of the H_3BTC linker.

3.8. Economic analysis and scalability

The cost assessment of the MARM-II adsorbent was performed, including the cost incurred for the MARM-II composite and the operational expenditures for treating a mixture of MLB, CNR, and LVX. Table S9 presents the chemical and energy costs involved in the synthesis of the MARM-II composite. The chemical costs were evaluated according to the current market value, while the energy cost was estimated based on the rate established by the West Bengal State Electricity Distribution Company Limited (WBSEDCL).[126] The total cost of the MARM-II composite was calculated to be 0.56 US $ per g. Furthermore, the use of a multi-point magnetic stirrer allows scaling opportunity with altered chemical cost while the energy cost remains

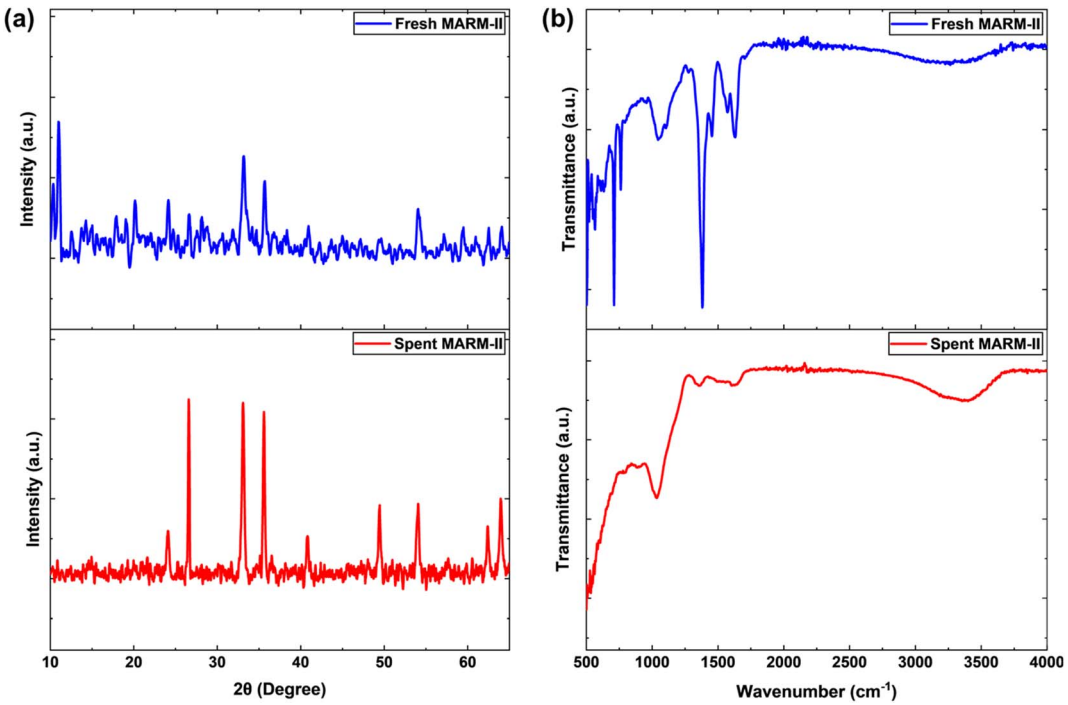

Fig. 10 (a) XRD, and (b) FTIR spectra of the fresh and spent MARM-II composite.

the same. This allows a cost reduction of about 53.6%, bringing it down to 0.27 US $ per g. In this context, the reported costs of similar MOF-based materials include MIL-100(Fe)–Fe^0 (0.19 US $ per g)[127] and MIL-100(Fe)-ore (0.11 US $ per g),[127] MIL-101(Cr) (4.28 US $ per g),[128] and UiO-66@kaolin (0.0716 US $ per g).[129] Furthermore, Biswal *et al.* (2021) reviewed that the production cost of similar adsorbents typically ranges between 0.1 and 5 US $ per g depending on the synthesis route.[130] Thus, the estimated cost of the present MARM-II adsorbent is within the reported range and remains competitive. The treatment cost (after scale-up) for a mixture of MLB, CNR, and LVX was calculated to be 0.13 US $ per L.

4. Summary and conclusions

The MARM-II composite was synthesized by integrating calcined RM during the preparation of MIL-100 (Fe) *via* co-precipitation. The as-prepared composite (MARM-II) was utilized for the adsorptive removal of MLB, CNR, and LVX from an aqueous solution. At the optimal condition (initial MLB, CNR, and LVX concentration: 10 mg L^{-1} each, MARM-II dose: 0.4 g L^{-1}, and solution pH: 7, and temperature: 27 ± 3 °C), about 93%, 96%, and 90% of MLB, LVX, and CNR were removed. The PSO kinetic model and findings from thermodynamics study suggested that physisorption is the primary mechanism governing the adsorption of the specified pollutants onto the MARM-II composite. The adsorption isotherm study indicated that the Sips isotherm, which carries characteristics of both the Langmuir and the Freundlich isotherms, effectively describes the adsorption process. The Q_{max} for MLB, CNR, and LVX were obtained to be 123.021 ± 11.926, 143.934 ± 24.248, and 97.657 ± 5.686 mg g^{-1}, respectively. The remarkable adsorptive potential of MARM-II is ascribed to its enhanced SSA, which provides abundant adsorptive sites, surface functional groups ($-COO^-$, –OH, $-NH_2$) that facilitate H-bonding and π–π interactions. The aforementioned features act synergistically to ensure multi-pollutant adsorption onto the MARM-II surface. The thermodynamic investigation indicated that the adsorption of the aforementioned pollutants occurs as an exothermic and spontaneous process. The adsorptive process was largely affected in the presence of HCO_3- ions, owing to their competition with the adsorbate molecules for the available adsorptive sites. The desorption and reusability study demonstrated that the MARM-II composite can be efficiently utilized for up to five cycles, showcasing its regenerative potential. This study advocates for the sustainable use of red mud, converting it into a valuable resource, specifically an effective adsorbent for the remediation of organic pollutants in water and wastewater, thus resulting in both water quality improvements and the reuse of waste materials.

Author contributions

Adarsh Singh: writing – original draft, validation, methodology, investigation, formal analysis, data curation, conceptualization. Manne Chimyang: writing – original draft, validation, methodology, investigation, formal analysis, data curation, conceptualization. Akash Rawat: writing – original draft, validation, methodology, investigation, formal analysis, data curation, conceptualization. Venkatesh Uddameri: writing – review & editing, visualization, supervision, methodology, conceptualization. Ashok Kumar Gupta: writing – review & editing, visualization, supervision, methodology, conceptualization.

Conflicts of interest

There are no conflicts of interest to declare.

Data availability

The data that support the findings of this study are available from the corresponding author upon reasonable request.

Supplementary information (SI) is available. See DOI: https://doi.org/10.1039/d6ra00635c.

Acknowledgements

Adarsh Singh, Manne Chimyang, and Akash Rawat are thankful to the Indian Institute of Technology Kharagpur, India, for the financial support.

References

1 A. Rawat, A. Srivastava, A. Bhatnagar and A. K. Gupta, *J. Cleaner Prod.*, 2023, **383**, 135382.
2 S. Boddu, M. Chavali, J. B. Dulla, V. N. Allugunulla, I. Mikkili, S. Malladi, S. Mannepalli and A. A. Khan, *Biomass Convers. Biorefin.*, 2025, **15**, 15399–15415.
3 N. Hanna, P. Sun, Q. Sun, X. Li, X. Yang, X. Ji, H. Zou, J. Ottoson, L. E. Nilsson, B. Berglund, O. J. Dyar, A. J. Tamhankar and C. Stålsby Lundborg, *Environ. Int.*, 2018, **114**, 131–142.
4 A. Ellafi, A. Dali, S. Mnif and S. Ben Younes, *Catal. Lett.*, 2023, **153**, 3620–3633.
5 B. Chakraborty, L. Ray and S. Basu, *Desalin. Water Treat.*, 2016, **57**, 14077–14082.
6 A. Orzoł and A. I. Piotrowicz-Cieślak, *Environ. Sci. Pollut. Res.*, 2017, **24**, 22226–22240.
7 A. Kanwal, R. Rehman, M. Imran, G. Samin, M. M. Jahangir and S. Ali, *RSC Adv.*, 2023, **13**, 26455–26474.
8 R. O. Alves de Lima, A. P. Bazo, D. M. F. Salvadori, C. M. Rech, D. de Palma Oliveira and G. de Aragão Umbuzeiro, *Mutat. Res., Genet. Toxicol. Environ. Mutagen.*, 2007, **626**, 53–60.
9 V. Bhardwaj, T. Bhardwaj, K. Sharma, A. Gupta, S. Chauhan, S. S. Cameotra, S. Sharma, R. Gupta and P. Sharma, *RSC Adv.*, 2014, **4**, 24935–24943.
10 J.-Q. Xiong, M. B. Kurade and B.-H. Jeon, *Chem. Eng. J.*, 2017, **313**, 1251–1257.
11 G. Chaturvedi, A. Kaur, A. Umar, M. A. Khan, H. Algarni and S. K. Kansal, *J. Solid State Chem.*, 2020, **281**, 121029.
12 S. H. Mousavi, M. Yaghoobi and F. Asjadi, *Sci. Rep.*, 2024, **14**, 18505.
13 S. Kundu and A. K. Gupta, *Chem. Eng. J.*, 2006, **122**, 93–106.

14 S. Ayoob, A. K. Gupta, P. B. Bhakat and V. T. Bhat, *Chem. Eng. J.*, 2008, **140**, 6–14.
15 P. S. Ghosal and A. K. Gupta, *RSC Adv.*, 2015, **5**, 105889–105900.
16 Y. Pi, C. Duan, Y. Zhou, S. Sun, Z. Yin, H. Zhang, C. Liu and Y. Zhao, *J. Hazard. Mater.*, 2022, **424**, 127577.
17 A. Imessaoudene, S. Cheikh, A. Hadadi, N. Hamri, J.-C. Bollinger, A. Amrane, H. Tahraoui, A. Manseri and L. Mouni, *Separations*, 2023, **10**, 57.
18 K. Gupta and O. P. Khatri, *Chem. Eng. J.*, 2019, **378**, 122218.
19 S. Dutta, S. K. Srivastava, B. Gupta and A. K. Gupta, *ACS Appl. Mater. Interfaces*, 2021, **13**, 54324–54338.
20 Z. Yu, H. Chen, J. Zhang, W. Sun, T. Li, Z. Qiu and M. Younas, *Sep. Purif. Technol.*, 2025, **352**, 128108.
21 S. Zhu, H. Xu, M. S. Khan, M. Xia, F. Wang and Y. Chen, *Water Res.*, 2025, **272**, 122997.
22 Y. Chen, H. Xu, M. S. Khan, S. Han and S. Zhu, *Crit. Rev. Environ. Sci. Technol.*, 2025, **55**, 1097–1123.
23 A. Singh, S. K K, A. Bhatnagar and A. K. Gupta, *Sep. Purif. Technol.*, 2025, **353**, 128588.
24 S.-H. Huo and X.-P. Yan, *J. Mater. Chem.*, 2012, **22**, 7449.
25 L. Oar-Arteta, T. Wezendonk, X. Sun, F. Kapteijn and J. Gascon, *Mater. Chem. Front.*, 2017, **1**, 1709–1745.
26 T. Yang, Y. Teng, J. Wang, S. Jia, Y. Su, X. Li, L. Li and C. Wang, *New J. Chem.*, 2023, **47**, 3903–3909.
27 W. He, Z. Li, S. Lv, M. Niu, W. Zhou, J. Li, R. Lu, H. Gao, C. Pan and S. Zhang, *Chem. Eng. J.*, 2021, **409**, 128274.
28 A. Rawat, S. K. Srivastava, C. S. Tiwary and A. K. Gupta, *J. Mater. Chem. A*, 2025, **13**, 1271–1286.
29 F. Tan, M. Liu, K. Li, Y. Wang, J. Wang, X. Guo, G. Zhang and C. Song, *Chem. Eng. J.*, 2015, **281**, 360–367.
30 R. Wang, H. Xu, X. Liu, D. Fang, S. Wei and A.-N. Yu, *Surf. Interfaces*, 2022, **34**, 102325.
31 Y. Liu and R. Naidu, *Waste Manage.*, 2014, **34**, 2662–2673.
32 J. Jin, X. Liu, S. Yuan, P. Gao, Y. Li, H. Zhang and X. Meng, *J. Ind. Eng. Chem.*, 2021, **98**, 298–307.
33 S. Mesgari Abbasi, A. Rashidi, A. Ghorbani and G. Khalaj, *Ceram. Int.*, 2016, **42**, 16738–16743.
34 G. Power, M. Gräfe and C. Klauber, *Hydrometallurgy*, 2011, **108**, 33–45.
35 Y.-T. Xu, K.-C. Ren, Z.-M. Tao, D. K. Sam, E. Feng, X. Wang, G. Zhang, J. Wu and Y. Cao, *Green Chem.*, 2023, **25**, 589–595.
36 J. Carneiro, D. M. Tobaldi, W. Hajjaji, M. N. Capela, R. M. Novais, M. P. Seabra and J. A. Labrincha, *Ceram. Int.*, 2018, **44**, 4211–4219.
37 A. Singh and A. K. Gupta, *Environ. Sci. Nano*, 2026, **13**, 563–581.
38 W. Fang, Y. Zhou, M. Cheng, L. Zhang, T. Zhou, Q. Cen, B. Li and Z. Liu, *J. Mol. Liq.*, 2024, **407**, 125171.
39 Q. Wang, J. Chen, X. Li, X. Yang, Y. Wu, S. Li, Y. Ye, D. Wang, D. Wang and Z. Zheng, *Fuel Process. Technol.*, 2022, **233**, 107316.
40 T. Steenhaut, S. Hermans and Y. Filinchuk, *New J. Chem.*, 2020, **44**, 3847–3855.
41 E. S. Dragan, D. F. Apopei Loghin and A. I. Cocarta, *ACS Appl. Mater. Interfaces*, 2014, **6**, 16577–16592.
42 Y. S. Ho and G. Mckay, *Can. J. Chem. Eng.*, 1998, **76**, 822–827.
43 S. Y. Elovich and O. G. Larionov, *Bull. Acad. Sci. USSR, Div. Chem. Sci.*, 1962, **11**, 191–197.
44 W. J. Weber and J. C. Morris, *J. Sanit. Eng. Div.*, 1963, **89**, 31–59.
45 I. Langmuir, *J. Am. Chem. Soc.*, 1918, **40**, 1361–1403.
46 H. Freundlich and W. Heller, *J. Am. Chem. Soc.*, 1939, **61**, 2228–2230.
47 R. Sips, *J. Chem. Phys.*, 1948, **16**, 490–495.
48 O. Redlich and D. L. Peterson, *J. Phys. Chem.*, 1959, **63**, 1024.
49 C. Chen, M. Zhang, Q. Guan and W. Li, *Chem. Eng. J.*, 2012, **183**, 60–67.
50 E. C. Lima, A. Hosseini-Bandegharaei, J. C. Moreno-Piraján and I. Anastopoulos, *J. Mol. Liq.*, 2019, **273**, 425–434.
51 J. Saleem, Z. K. B. Moghal, S. Pradhan and G. McKay, *RSC Adv.*, 2024, **14**, 33797–33808.
52 A. Dhakshinamoorthy, M. Alvaro, Y. K. Hwang, Y.-K. Seo, A. Corma and H. Garcia, *Dalton Trans.*, 2011, **40**, 10719.
53 C. Brahmi, M. Benltifa, C. Vaulot, L. Michelin, F. Dumur, E. Gkaniatsou, C. Sicard, A. Airoudj, F. Morlet-Savary, L. Bousselmi and J. Lalevée, *ChemistrySelect*, 2021, **6**, 8120–8132.
54 M. A. El-Aal, A. E.-A. A. Said, M. H. Abdallah and M. N. Goda, *Sci. Rep.*, 2022, **12**, 9407.
55 Y. Chen, S. Gao, E. J. Jones and B. Singh, *Environ. Sci. Technol.*, 2021, **55**, 4629–4637.
56 Q. Li, G. Wei, Y. Yang, Z. Li, L. Zhang and Q. Huang, *J. Hazard. Mater.*, 2020, **394**, 122566.
57 J. Zan, H. Song, S. Zuo, X. Chen, D. Xia and D. Li, *J. Cleaner Prod.*, 2020, **246**, 118971.
58 H. Li, F. Liu, X. Ma, Z. Wu, Y. Li, L. Zhang, S. Zhou and Y. Helian, *Energy Convers. Manage.*, 2019, **180**, 401–410.
59 Q. Li, X. Luo, J. Cai, G. Li, P. Wang, W. Han and Y. Lan, *J. Catal.*, 2024, **436**, 115625.
60 J.-G. Lee, B. N. Joshi, E. Samuel, S. An, M. T. Swihart, J. S. Lee, Y. K. Hwang, J.-S. Chang and S. S. Yoon, *J. Alloys Compd.*, 2017, **722**, 996–1001.
61 K. Vinothkumar and R. G. Balakrishna, *Appl. Catal., B*, 2024, **340**, 123199.
62 A. Ene, S. S. Moraru, D. I. Moraru, A. Pantelica, S. Gosav and A. M. Ceoromila, *Appl. Sci.*, 2024, **14**, 5616.
63 K. D. Nguyen, T. T. Thu, A. T. H. Tran, O. T. K. Le, S. Sagadevan and N. H. Mohd Kaus, *ACS Omega*, 2023, **8**, 41258–41272.
64 A. Čiuladienė, A. Luckutė, J. Kiuberis and A. Kareiva, *Chemija*, 2018, **29**, 243–256.
65 M. A. Al-Kazragi, D. T. A. Al-Heetimi and O. S. A. Al-Khazrajy, *Desalin. Water Treat.*, 2019, **145**, 369–377.
66 P. Sarawade, H. Tan, D. Anjum, D. Cha and V. Polshettiwar, *ChemSusChem*, 2014, **7**, 529–535.
67 Y. J. C. Martins, A. C. M. Almeida, B. M. Viegas, R. A. do Nascimento and N. F. da P. Ribeiro, *Int. J. Environ. Sci. Technol.*, 2020, **17**, 4133–4148.
68 H. Shi, Z. Gu, M. Han, C. Chen, Z. Chen, J. Ding, Q. Wang, H. Wan and G. Guan, *Colloids Surf., A*, 2021, **608**, 125585.

69 F. Lian, C. Chang, Y. Du, L. Zhu, B. Xing and C. Liu, *J. Environ. Sci.*, 2012, **24**, 1549–1558.
70 D. Liu, D. Zou, H. Zhu and J. Zhang, *Small*, 2018, **14**, 1801454.
71 *Hierarchically Structured Porous Materials*, ed. B. Su, C. Sanchez and X. Yang, Wiley, 2011.
72 H. Weng, P. Zhang, Z. Guo, G. Chen, W. Shen, J. Chen, X. Zhao and M. Lin, *ACS Appl. Mater. Interfaces*, 2021, **13**, 8249–8262.
73 J. J. Delgado-Marín, J. Narciso and E. V. Ramos-Fernández, *Materials*, 2022, **15**, 6499.
74 V. K. Singh, A. Sett and S. Karmakar, *Chem. Eng. J.*, 2024, **481**, 148373.
75 S. Kim, P. Anushkkaran, W.-S. Chae, S. H. Choi, M. Kumar, M. Cho, M. A. Mahadik, H. H. Lee and J. S. Jang, *ACS Appl. Energy Mater.*, 2022, **5**, 915–929.
76 H. Wang, J. Di, Y. Sun, J. Fu, Z. Wei, H. Matsui, A. del C. Alonso and S. Zhou, *Adv. Funct. Mater.*, 2015, **25**, 5537–5547.
77 *NIST X-Ray Photoelectron Spectroscopy Database (SRD 20)*, Version 5.0.
78 C. Dhanasekhar, S. K. Mishra, R. Rawat, A. K. Das and A. Venimadhav, *J. Alloys Compd.*, 2017, **726**, 148–153.
79 P. Zhang, J. Wu, Y. Wang, H. Sarvari, D. Liu, Z. D. Chen and S. Li, *J. Mater. Chem. A*, 2017, **5**, 17368–17378.
80 M. Du, J. Zhang, J. Rong, T. Peng, Y. Chen, Y. Ji and Y. Guan, *MRS Commun.*, 2024, **14**, 1371–1379.
81 B. Zhao, X. Fu, Y. Di, L. Wei, G. Shao, H. Cui, L. Wei, N. Liu, Q. An and S. Zhai, *J. Mol. Struct.*, 2024, **1312**, 138619.
82 R. Narukulla, U. Ojha and T. Sharma, *Colloids Surf., A*, 2022, **641**, 128594.
83 Q. Wu, W. Luo, Y. Du, Y. Yang, Y. Xiao, N. Cheng, B. Tang, H. Li, L. Wang, D. Wang, C. Wang, J. Guan and X. Shen, *Biomacromolecules*, 2023, **24**, 3522–3531.
84 A. Xie, L. Cao, T. Shen, Y. Zhou, H. Wang and S. Luo, *Microchem. J.*, 2024, **204**, 111101.
85 N. U. Qadir, S. A. M. Said, R. B. Mansour, K. Mezghani and A. Ul-Hamid, *Dalton Trans.*, 2016, **45**, 15621–15633.
86 Y.-K. Seo, J. W. Yoon, J. S. Lee, U.-H. Lee, Y. K. Hwang, C.-H. Jun, P. Horcajada, C. Serre and J.-S. Chang, *Microporous Mesoporous Mater.*, 2012, **157**, 137–145.
87 R. C. Sahu, R. Patel and B. C. Ray, *Fuel Process. Technol.*, 2011, **92**, 1587–1592.
88 I. Bezverkhyy, E. Popova, N. Geoffroy, F. Herbst and J.-P. Bellat, *J. Mater. Chem. A*, 2016, **4**, 8141–8148.
89 S. Basu, G. Ghosh and S. Saha, *Process Saf. Environ. Prot.*, 2018, **117**, 125–142.
90 V. Basavarao and S. Rammohanrao, *Chem. Eng. J.*, 2006, **116**, 77–84.
91 M. H. Dehghani, M. Ghadermazi, A. Bhatnagar, P. Sadighara, G. Jahed-Khaniki, B. Heibati and G. McKay, *J. Environ. Chem. Eng.*, 2016, **4**, 2647–2655.
92 Y. Liu, G. Qiu, Y. Liu, Y. Niu, R. Qu, C. Ji, Y. Wang, Y. Zhang and C. Sun, *J. Mol. Liq.*, 2022, **360**, 119405.
93 L. P. Lingamdinne, G. K. R. Angaru, B. Shrestha, J. R. Koduru and R. R. Karri, *Sci. Rep.*, 2026, **16**, 7794.
94 S. Sudarsan, G. Murugesan, T. Varadavenkatesan, R. Vinayagam and R. Selvaraj, *Sci. Rep.*, 2025, **15**, 1831.
95 T. H. Ho, H. D. Tong and T. T. Trinh, *Chem. Eng. J. Adv.*, 2026, **25**, 101017.
96 S. E. Moradi, S. Dadfarnia, A. M. Haji Shabani and S. Emami, *Desalin. Water Treat.*, 2015, **56**, 709–721.
97 G. Hähner, A. Marti, N. D. Spencer and W. R. Caseri, *J. Chem. Phys.*, 1996, **104**, 7749–7757.
98 J. J. Salazar-Rabago, R. Leyva-Ramos, J. Rivera-Utrilla, R. Ocampo-Perez and F. J. Cerino-Cordova, *Sustainable Environ. Res.*, 2017, **27**, 32–40.
99 R. Song, J. Yao, M. Yang and Z. Ye, *Langmuir*, 2022, **38**, 9400–9409.
100 F. Hasanvandian, A. Shokri, M. Moradi, B. Kakavandi and S. Rahman Setayesh, *J. Hazard. Mater.*, 2022, **423**, 127090.
101 W. Li, T. Zhang, L. Lv, Y. Chen, W. Tang and S. Tang, *Colloids Surf., A*, 2021, **624**, 126791.
102 G. M. Sawood, A. Mishra and S. K. Gupta, *J. Hazard., Toxic Radioact. Waste*, 2021, **25**, 04020075.
103 N. Y. Acelas, C. Hadad, A. Restrepo, C. Ibarguen and E. Flórez, *Inorg. Chem.*, 2017, **56**, 5455–5464.
104 Q. Zheng, Y. Luo and Z. Luo, *Environ. Sci. Pollut. Res.*, 2022, **30**, 27241–27256.
105 R. J. Martin and K. O. Iwuco, *Water Res.*, 1982, **16**, 73–82.
106 Y. Aldegs, M. Elbarghouthi, A. Elsheikh and G. Walker, *Dyes Pigm.*, 2008, **77**, 16–23.
107 X. Zheng, Z. Xu, J. Liu, Y. Luo, L. Gu, D. Zhao, S. Hu and X. Pan, *Carbon Res.*, 2022, **1**, 27.
108 W. Li, P. Zuo, D. Xu, Y. Xu, K. Wang, Y. Bai and H. Ma, *Chem. Eng. Res. Des.*, 2017, **124**, 260–270.
109 A. Thakur, H. Assad, S. Kaya and A. Kumar, in *Eco-Friendly Corrosion Inhibitors*, Elsevier, 2022, pp. 283–310.
110 X. Huang, N. Gao and Q. Zhang, *J. Environ. Sci.*, 2007, **19**, 1287–1292.
111 W. A. El-Mehalmey, A. Helmy, M. A. Seleem, M. Amin, A. S. Mayhoub and M. H. Alkordi, *J. Mater. Chem. A*, 2025, **13**, 22563–22573.
112 S. Sivalingam and A. S, *Environ. Sci. Adv.*, 2024, **3**, 732–750.
113 P. Liu, Z. Wu, X. Ge and X. Yang, *RSC Adv.*, 2019, **9**, 11696–11706.
114 S. Mohamed Nasser, M. Abbas and M. Trari, *Prog. React. Kinet. Mech.*, 2024, **49**, 14686783241226858.
115 É. C. Lima, M. A. Adebayo and F. M. Machado, 2015, *Kinetic and Equilibrium Models of Adsorption*, pp. 33–69.
116 H. Lachheb, E. Puzenat, A. Houas, M. Ksibi, E. Elaloui, C. Guillard and J.-M. Herrmann, *Appl. Catal., B*, 2002, **39**, 75–90.
117 Z. A. Jamiu, T. A. Saleh and S. A. Ali, *RSC Adv.*, 2015, **5**, 42222–42232.
118 E. Wibowo, M. Rokhmat, Sutisna, Khairurrijal and M. Abdullah, *Desalination*, 2017, **409**, 146–156.
119 K. Wu, Q. Nan and T. Wu, *Complexity*, 2020, **2020**, 1–11.
120 T. E. Khalil, E. El-Meligy, L. A. Mohamed, A. El-dissouky and M. Amer, *Int. J. Biol. Macromol.*, 2025, **318**, 145335.
121 F. Khalili and G. Al-Banna, *J. Environ. Radioact.*, 2015, **146**, 16–26.

122 M. G. Oliveira, M. P. Spaolonzi, E. D. V. Duarte, H. P. S. Costa, M. G. C. da Silva and M. G. A. Vieira, *Environ. Res.*, 2023, **233**, 116503.
123 E. Duque-Brito, D. R. Lobato-Peralta, J. A. Okolie, D. M. Arias, P. J. Sebastian and P. U. Okoye, *Energy, Ecol. Environ.*, 2024, **9**, 84–99.
124 S. Bentahar, A. Dbik, M. El Khomri, N. El Messaoudi and A. Lacherai, *J. Environ. Chem. Eng.*, 2017, **5**, 5921–5932.
125 BIS, *IS 10500: 2012, Indian Standard Drinking Water — Specification (Second Revision)*, New Delhi 110002, 2012.
126 WBSEDCL, *Tariff Rate for the Year 2024-25*, 2025.
127 M. Chang, C. Tang, C.-C. Wang and C. Zhao, *Prog. Nat. Sci.:Mater. Int.*, 2024, **34**, 66–73.
128 A. A. Rico-Barragán, J. R. Álvarez, S. Pioquinto-García, J. Rodríguez-Hernández, P. Rivas-García and N. E. Dávila-Guzmán, *Sustainable Prod. Consumption*, 2023, **40**, 159–168.
129 N. Kanmaz, *Environ. Res. Technol.*, 2025, **8**, 581–592.
130 L. Biswal, J. E. Goodwill, C. Janiak and S. Chatterjee, *Sep. Purif. Rev.*, 2022, **51**, 408–426.
131 *PubChem, PubChem Compound – NCB*, accessed 21 September 2025, https://pubchem.ncbi.nlm.nih.gov/.